

Ice chemistry in starless molecular cores

J. Kalvāns

*Engineering Research Institute "Ventspils International Radio Astronomy Center" of Ventspils University
College, Inženieru 101, Ventspils, Latvia, LV-3601*

juris.kalvans@venta.lv

ABSTRACT

Starless molecular cores are natural laboratories for interstellar molecular chemistry research. The chemistry of ices in such objects was investigated with a three-phase (gas, surface, and mantle) model. We considered the center part of five starless cores, with their physical conditions derived from observations. The ice chemistry of oxygen, nitrogen, sulfur, and complex organic molecules (COMs) was analyzed. We found that an ice-depth dimension, measured, e.g., in monolayers, is essential for modeling of chemistry in interstellar ices. Particularly, the $\text{H}_2\text{O}:\text{CO}:\text{CO}_2:\text{N}_2:\text{NH}_3$ ice abundance ratio regulates the production and destruction of minor species. It is suggested that photodesorption during core collapse period is responsible for high abundance of interstellar H_2O_2 and O_2H , and other species synthesized on the surface. The calculated abundances of COMs in ice were compared to observed gas-phase values. Smaller activation barriers for CO and H_2CO hydrogenation may help explain the production of a number of COMs. The observed abundance of methyl formate HCOOCH_3 could be reproduced with a 1kyr, 20K temperature spike. Possible desorption mechanisms, relevant for COMs, are gas turbulence (ice exposure to interstellar photons) or a weak shock within the cloud core (grain collisions). To reproduce the observed COM abundances with the present 0D model, 1-10% of ice mass needs to be sublimated. We estimate that the lifetime for starless cores likely does not exceed 1Myr. Taurus cores are likely to be younger than their counterparts in most other clouds.

Subject headings: astrochemistry — molecular processes — ISM: clouds — ISM: abundances — ISM: individual objects (CB 17, CB 26, CB 27, B 68)

1. Introduction

Low-mass interstellar molecular clouds, such as the Bok globules, are a model case for cloud structure and star-formation studies, thanks to their relative simplicity and proximity (Hartmann 2009). For astrochemistry, stable starless cores within these clouds are particularly interesting. They are sufficiently dense for a significant mass of ice to accumulate onto the grains, supposedly not disturbed by gravitational contraction motions. Thus, modeling of surface chemistry can be simplified to calculations that consider constant, yet realistic physical conditions.

The aim of the present paper is to study the evolution of the chemical composition of ices in starless cores with physical conditions that are

relevant to actual cores. The modeling of surface chemistry in starless cores has a long history. Important papers that have presented significant advances in the field include Watson & Salpeter (1972); Allen & Robinson (1977); Pickles & Williams (1977a,b); Tielens & Hagen (1982); D'Hendecourt et al. (1985); Brown & Millar (1989); Brown (1990); Hasegawa et al. (1992). A model for small, diffuse clouds (not the starless core) with surface chemistry has been presented by Turner (1998). Such two-phase models with constant physical parameters have also been used in recent papers (e.g., Du et al. 2012; Vasyunin & Herbst 2013b).

Starless cores with physical conditions derived from actual observations have also been modeled (Du et al. 2012; Maret et al. 2013; Lippok et al.

2013; Awad et al. 2014). Recent advances in the field of interstellar ice chemistry in combination with available observational data (e.g. Launhardt et al. 2010) make the modeling of ices in quiescent cores an interesting proposal. These advances include ices described as consisting of layers, with only the surface monolayer (ML) being available for reactions (Hasegawa & Herbst 1993b; Bergin & Langer 1997; Cuppen & Herbst 2007; Garrod & Pauly 2011; Taquet et al. 2012), photoprocessing of subsurface ices (Kalvāns & Shmeld 2010; Garrod 2013; Chang & Herbst 2014), and a realistic model of ice molecule formation.

An important aspect in interstellar ice models is a proper description of surface reactions in a *contracting* molecular core. Notably, this includes the surface synthesis of CO₂ (Ruffle & Herbst 2001b; Garrod & Pauly 2011). Brown et al. (1988) and Aikawa et al. (2001) show that the contraction phase is particularly important for a correct representation of the ice formation epoch. Recent dense core models that focus on surface chemistry often do not consider the core contraction phase (Du et al. 2012; Kalvāns & Shmeld 2013; Vasyunin & Herbst 2013b; Chang & Herbst 2014; Reboussin et al. 2014). The dependence of ice composition on the core density and interstellar extinction has been shown by a number of earlier studies (e.g., Rawlings et al. 1992; Viti & Williams 1999; Green et al. 2001).

We studied four starless cores – CB 17 - SMM1, CB 26 - SMM, CB 27 - SMM, and B 68 – with chemical kinetics modeling. They were treated as clumps of gas and dust with an increased density towards the center, surrounded by a more diffuse cloud. The cores undergo an initial contraction phase, until they reach a state with constant (observed) physical conditions (section 2.1). A detailed surface and subsurface ice chemistry model has been used (2.2), whose application to starless cores is the main novelty of this paper.

2. Methods

The model ‘Alchemic-Venta’ was employed in this research, taken from previous works (Kalvāns 2015a,b, hereafter Papers I and II, respectively). It is based on the ‘ALCHEMIC’ code (Semenov et al. 2010), with details explained below. Physical parameters in the model were ad-

justed for a selection of non-starforming cores. Papers I and II investigate collapsing prestellar cores, while the present paper focuses on stable, non-starforming cores.

2.1. Physical model

2.1.1. Cloud core conditions

We investigate ice chemistry of four starless cores with their central density $n_{\text{H}} = n(\text{H}) + 2n(\text{H}_2)$, cm⁻³, and interstellar extinction A_V , mag, derived from observations. Only the core center part was considered (i.e., 0D model), where n_{H} and A_V are at their highest. Each simulation consists of a collapse Phase 1, when the cloud density increases, and a quiescent Phase 2 with constant physical conditions.

A single-point 0D model was chosen because the ices in the center of each core most likely do exist, despite a number of uncertain parameters. These include the efficiency of non-thermal desorption mechanisms and turbulent motions in starless cores, as observed by Redman et al. (2006); Levshakov et al. (2014), and Steinacker et al. (2014). Turbulence was not considered in the present study. Also, ices in core center likely have experienced the full range of physical conditions of the core since its formation. The simple 0D model puts certain constraints for the interpretation of results.

Cores with a Plummer-like density profile (Plummer 1911; Whitworth & Ward-Thompson 2001), embedded in a surrounding cloud with a fixed column density N_{out} , were modeled. The

Table 2: Initial abundances of chemical species.

Species	n_i/n_{H}
H ₂	0.4995
H	1.00E-03
He	9.00E-02
C	1.40E-04
N	7.50E-05
O	3.20E-04
Na	2.00E-08
Mg	2.55E-06
Si	1.95E-06
P	7.63E-08
S	1.50E-06
Cl	1.40E-08
Fe	7.40E-07

Table 1: The constant physical parameters of modeled starless cores during their stable Phase 2.

Core	Observational data						Calculated data		
	$n_{\text{H},0}$, cm^{-3}	r_0 , AU	r_1 , AU	η	N_{out} , cm^{-2}	Ref.	A_V , mag	T , K	t_1 , kyr
CB 17 S - SMM1	2.3E+5	9.5E+3	3.0E+4	4.9	0	S ^a	13.8	8.2	1465
CB 17 L - SMM	1.3E+5	1.1E+4	3.0E+4	5.0	3.6E+20	L ^b	9.1	9.2	1451
CB 26 - SMM	8.7E+4	8.0E+3	4.0E+4	3.0	2.2E+20	L	6.5	11.1	1437
CB 27 - SMM	1.3E+5	1.3E+4	6.6E+4	6.0	3.1E+20	L	9.5	8.9	1451
B 68 - SMM	4.0E+5	7.0E+3	2.7E+4	5.0	3.0E+20	L	17.6	7.9	1482

NOTE.—Assumed physical parameters: $n_{\text{H},0}$ —density at the center of the core; r_0 —radius of the central density plateau; η —power-law slope for density; r_1 —radius of the region (core) in consideration; N_{out} —column density of the surrounding cloud. Calculated parameter t_1 is the length of the cloud core collapse Phase 1.

^aSchmalzl et al. (2014)

^bLippok et al. (2013)

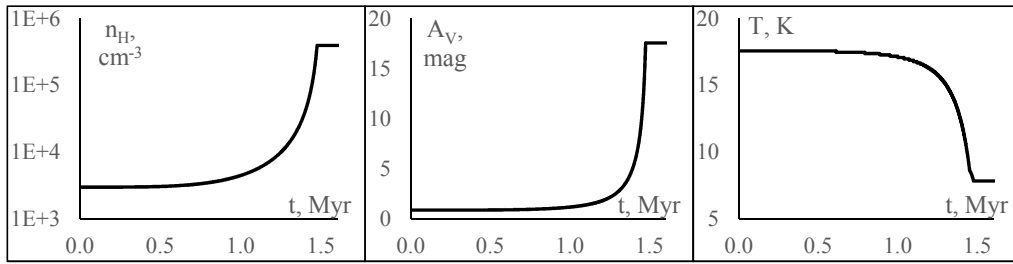


Fig. 1.— Density of hydrogen atoms, interstellar extinction, and temperature of the B 68 SMM cloud core – an example of the evolution of physical conditions during the contraction Phase 1. After the contraction phase, these parameters were allowed to remain unchanged for a total integration time of 3.5 Myr.

total column density to the core center can be calculated with

$$N_H = \int_{r_1}^0 \frac{n_{H,0}}{[1 + (r/r_0)^2]^{\eta/2}} dr + N_{\text{out}}, \text{cm}^{-2}, \quad (1)$$

where $n_{H,0}$ is the (maximum) density at the center of the core, r_0 is the radius of the central density plateau, η is the power-law slope at large radii, and r_1 is the radius of the core. The chemical modeling was done only for the center of the core, where $r = 0$ and the density profile of the core is necessary only for the calculation of N_H at its center. Table 1 summarizes the parameters $n_{H,0}$, r_0 , r_1 , and N_{out} . These are unique for each core, and were derived from Lippok et al. (2013) for the CB 17, CB 26, CB 27, and B 68 cores and from Schmalzl et al. (2014) for the CB 17 core. The two ‘versions’ of CB 17 are hereafter denoted CB 17 S and CB 17 L, for data from Schmalzl et al. and Lippok et al., respectively. This means that there are a total five models (CB 17 S, CB 17 L, CB 26, CB 27, and B 68) of four cores considered.

Table 1 data are relevant to cores in the stable Phase 2, when the contraction in Phase 1 has ended and the physical parameters of the cores are unchanging. This phase has an assumed integration time of $t_2 > 2\text{Myr}$ for each modeled core. Prior to the stable phase, a core formation phase was considered. The formation of starless cores have been described before as a free-fall (e.g., Lee et al. 2004) or ‘delayed free-fall’ (e.g., Taquet et al. 2014). A ‘static’, step-like contraction was employed by these authors.

In the present study, the formation of the core was described as a delayed free-fall process. The approach presented by Brown et al. (1988), Nejad et al. (1990) and Rawlings et al. (1992) was used. A Plummer-like core with an initial peak density of $n_{H,\text{ini}} = 3000\text{cm}^{-3}$ contracts to the final density $n_{H,0}$ in a core formation time t_1 (i.e., length of Phase 1, see Table 1). The parameter B in equation (1) of Rawlings et al. (1992), which modifies the rate of the contraction, was taken to be $2/3$. This means that the collapse to the final densities, indicated in Table 1, occurs in 1.4-1.5Myrs. Figure 1 shows an example of the evolution of physical conditions for a core (B 68) during the contraction phase, up to 1.5Myr.

A value $B = 0.7$ has been used by Nejad et al. (1990), Rawlings et al. (1992), and Ruffle et al.

(1999) for prestellar core models. We take $B = 2/3$ as a somewhat lower value for starless cores. The exact value of B has only a limited effect on ice composition, the main subject of the present study. This is because ice accumulation was calibrated by modifying the poorly-known efficiency of indirect reactive desorption to match the observed proportions of H_2O , CO , and CO_2 (section 2.1.4).

For the core formation epoch, r_0 was kept proportional to $n_{H,0}^{-1/2}$ (Keto & Caselli 2010; Taquet et al. 2014). The Plummer-like density profile of the contracting core was retained, while the density increases from $n_{H,\text{ini}}$ to $n_{H,0}$. The value of r_1 , which determines the physical size of the region in consideration, was assumed constant. This means that the mass of the core (i.e., the number of H atoms within a sphere of radius r_1) increases during the formation phase. N_{out} was retained constant, too.

The total integration time $t_1 + t_2$ was taken to be 3.5Myr and the results were analyzed for an interval of 1.0-2.3Myr (see section 3.3). In context with ice formation, the full time consists of three periods: (1) cloud with $n_{H,0} \approx 3 \times 10^3\text{cm}^{-3}$ and no ice on the grains; (2) ice accumulation up to a maximum thickness in a rapidly contracting core and up to 200kyr into the quiescent phase; (3) slow processing of ice by cosmic-ray induced photons after the freeze-out has ceased. The start of period (2) is marked with the appearance of first subsurface ice species at densities 5×10^3 to $1 \times 10^4\text{cm}^{-3}$. During the last period (3) the gas and the surface are in an approximate adsorption-desorption equilibrium. The nominal ice thickness decreases during period (3).

Ice photoprocessing leads to a declining amount of CO in the icy mantles. Because of this, quiescent Phase 2 integration times longer than 2Myr were not considered. For longer times, the $\text{H}_2\text{O}:\text{CO}:\text{CO}_2$ ice abundance ratio is no longer supported by observations of interstellar ices (Gibb et al. 2004; Whittet et al. 2007; Boogert et al. 2011; Öberg et al. 2011). Mantle growth and the abundances of major ice species are considered in section 3.

Gas and dust were assumed to be in thermal equilibrium with temperature derived from the interstellar extinction A_V , in line with Garrod & Pauly

(2011). In other words, it was assumed that the cores are heated externally by the interstellar radiation field. A_V was calculated with:

$$A_V = \frac{N_H}{1.60 \times 10^{21}}, \quad (2)$$

Table 1 shows the calculated values for A_V and T for each of the modeled cores in the stable phase.

Table 2 shows the chemical abundances used at the start for all simulations. They are based on the abundances derived by Garrod & Herbst (2006) and Wakelam & Herbst (2008). The rate of hydrogen ionization by cosmic rays was taken to be $1.3 \times 10^{-17} \text{s}^{-1}$. The flux of cosmic-ray induced photons and interstellar photons was taken to be 4875 and $10^8 \text{cm}^{-2} \text{s}^{-1}$, respectively, with a grain albedo of 0.5 .

The self- and mutual-shielding of H_2 , CO , and N_2 was included with the use of the tabulated shielding functions (Lee et al. 1996; Li et al. 2013). Shielding was also attributed to molecules in ice. It is important to note that the surrounding molecular cloud was included in these calculations by assuming an external H_2 column density of $N_{\text{out}}/2$. This was not included in Papers I and II that used a physical model built on similar principles. Such more accurate approach here is of particular importance, because more plausible values for indirect reactive desorption efficiency can now be derived (section 2.1.4). The synthesis of hydrogen on grain surface was considered by, both, Langmuir-Hinshelwood and Eley-Rideal mechanisms, although the latter is of little importance.

2.1.2. Dust grain properties

The grains were assumed to consist of two components. The first is inert, solid nuclei with a radius of $a = 0.1 \mu\text{m}$ and an abundance 1.32×10^{-12} relative to H atoms. In dark and dense conditions ($A_V > 1.9 \text{mag}$), the second component, interstellar ice, begins to accumulate onto grain surfaces in significant amounts. The increase of grain size is calculated self-consistently, assuming a thickness of 350pm for each ML, which is multiplied by the number of ice MLs to obtain ice thickness b . The number of adsorption sites per ML was retained constant at 1.5×10^6 . Changes in this number likely do not influence the agreement of model results with observations (Acharyya et al.

2011; Taquet et al. 2012), and were not considered in the model. Dust grain albedo was assumed to be 0.5 .

The ice layer on the grains was described with the sublayer approach, developed in Paper II. This means that a fully formed ice (accumulation from gas has ceased) consists of a surface layer (1-2 MLs) and three subsurface layers – ‘sublayers’ – of approximately equal thickness. A sublayer nominally may contain up to several tens of MLs. Two or more sublayers in a model allow to consider the depth-dependent composition of the ice mantles. Three sublayers were considered in the present study, similarly to Paper II. For reference, they were numbered with the first being the shallowest and the third being the sublayer adjacent to grain nucleus. The transition from surface to the first sublayer and, subsequently, to second and third sublayers has been harmonized with the accretion rate, in line with Papers I and II.

2.1.3. Ice physical description

The molecules are bound to the surface or into the mantle with their adsorption (E_D) or absorption energies (E_B), respectively. E_D is the ‘basic value’, given in the reaction network, from which all the other energies were calculated. The binding energies, used for calculating the diffusion rates, for surface ($E_{b,S}$) and mantle ($E_{b,M}$) species were assumed to be $0.40E_D$ and $0.40E_B$, respectively (Garrod & Pauly 2011). In Papers I and II it was argued that $E_{b,M}$ has to be higher, or similar to E_D , otherwise the movement of molecules in ice bulk would be faster than their evaporation from surface, which fits the description of a liquid, not solid. In line with the earlier works, it was assumed that $E_B = 3E_D$, i.e., that typically $E_{b,M} = 1.2E_D$. For CO and CO_2 molecules, the ratios $E_{b,S}/E_D = E_{b,M}/E_B$ were taken to be 0.31 and 0.39 , respectively (Karssemeijer & Cuppen 2014).

In dark cores, the grains may be sufficiently cold to have a significant proportion of their surface covered by molecular hydrogen. H_2 provides a much weaker binding than water ice. The adsorption energy for H and H_2 was calculated according to Garrod & Pauly (2011). For other species, E_D was not affected by the surface coverage of H_2 because of the large difference between the hopping rate of H_2 and vibration frequency of heavy molecules (Paper II).

Accretion of neutral gaseous species onto the grains with a radius $a+b$ was calculated with sticking probabilities of 0.33 for light species (H, H₂) and 1.0 for all other species (Kalvāns & Shmied 2010). A total of six desorption mechanisms were considered. The rate coefficients for evaporation and cosmic-ray-induced whole-grain heating (Hasegawa & Herbst 1993a) were calculated for each molecule as a thermal desorption at the equilibrium temperature and 70K, respectively. Desorption by interstellar and cosmic-ray-induced photons was considered with uniform yields for all species, 0.003 and 0.002, respectively. These values were chosen to be in agreement with recent photodesorption experiments with interstellar ice analogs, as discussed in Paper II. Photodesorption from subsurface mantle species was permitted, if the number of overlying MLs does not exceed two. The yield for subsurface photodesorption was reduced by a factor of 1/3. This approach was developed to be in line with the results of Andersson & van Dishoeck (2008).

A reaction-specific reactive desorption was used, with the α_{RRK} parameter set to 0.03 (Paper II). This is the ratio of the surface-molecule bond frequency to the frequency at which energy is lost to the grain surface (Garrod et al. 2007).

2.1.4. Indirect reactive desorption

Desorption induced by the energy released from the H+H exothermic surface reaction probably determines the relative proportions of major ice components H₂O, CO, and CO₂. In order to reproduce observations of interstellar ices, a sequence CO > CO₂ >> H₂O must be observed for indirect reactive desorption efficiency $f_{\text{H}_2\text{fd}}$ (Paper II). Without indirect reactive desorption, the calculated abundance of solid carbon species in collapsing cores can be overestimated, when compared to the observational results provided by Gibb et al. (2004); Whittet et al. (2007), and Öberg et al. (2011). For example, realistic CO and CO₂ relative abundances can be achieved, if the ice contains a substantial amount of CH₄, H₂CO, and (or) CH₃OH (Garrod & Pauly 2011; Taquet et al. 2014). Of the latter three species only methanol has been occasionally observed in interstellar ices (Boogert et al. 2011).

The parameter $f_{\text{H}_2\text{fd}}$ can be described as the number of desorbed molecules per H₂ formed on a

grain. Exact value for the efficiency are unknown, and, given the averaging and uncertainties in astrochemical numerical simulations, it is reasonable to adjust $f_{\text{H}_2\text{fd}}$ so that it produces an approximate fit with observations of starless cores. Such an approach can be used until a more precise value of $f_{\text{H}_2\text{fd}}$ is found in experiments or, for example, quantum chemistry calculations.

In order to derive $f_{\text{H}_2\text{fd}}$ for the present study, we employ a similar method to Paper II. A prestellar core in free-fall gravitational collapse was considered in that study. For the present research, the B 68 core model (Table 1) was used. It has the highest final density and final A_V among all the starless cores in consideration. This allows the comparison of observed/modeled CO:H₂O and CO₂:H₂O ice abundance ratios for five A_V values from the dataset of Whittet et al. (2007). An additional observational constraint for the model is the abundance of H₂O, CO, and CO₂ ices at their respective threshold extinctions A_{th} .

The above means that, while the B 68 cloud core is currently stable (Bergin et al. 2006; Redman et al. 2006), we assume that it formed in a delayed free-fall process, which ceased when the core reached its present density. This assumption has been attributed to all simulated cores in this study. While it might not be entirely correct, it is probably just as useful as other realistic assumptions, because of the poorly constrained value of $f_{\text{H}_2\text{fd}}$, which has to be calibrated, regardless of the exact core formation path.

Table 3 summarizes the observational and best-fit B 68 model results. The desorption efficiency $f_{\text{H}_2\text{fd}}$ was calculated according to the empiric approach of Paper II:

$$f_{\text{H}_2\text{fd}} = Q \exp(-E_D/(Q_1)), \quad (3)$$

where $Q = 9.5 \times 10^{-5}$ and $Q_1 = 10^3$. The adopted best-fit values of Q and Q_1 are different from those in Paper II. It is possible that the values obtained here are more reliable than those of Paper II because of the more advanced and realistic physical model (section 2.1.1).

The observational values for CO:H₂O and CO₂:H₂O ice abundance ratios were taken from Whittet et al. (2007). While newer datasets are available (Boogert et al. 2011; Öberg et al. 2011), Whittet et al. provides the A_V for each background star, which enables to tie the observations

Table 3: Comparison of observed and calculated (B 68 core) CO and CO₂ ice abundances, relative to water. Observational data from Whittet et al. (2007), unless noted otherwise.

Source ID	A_V	Observations		B 68 model		t^b , kyr
		$\frac{\text{CO}}{\text{H}_2\text{O}}^a$, %	$\frac{\text{CO}_2}{\text{H}_2\text{O}}$, %	$\frac{\text{CO}}{\text{H}_2\text{O}}$, %	$\frac{\text{CO}_2}{\text{H}_2\text{O}}$, %	
043728.2+261024	6.3 ± 1.5	. . .	25.0	1.8	13.8	1417
042324.6+250009	10.0 ± 0.5	20.2	19.1	7.7	13.0	1451
043325.9+261534	11.7 ± 0.5	12.0	16.7	12.5	13.9	1459
043926.9+255259	15.3 ± 0.5	27.3	16.7	30.2	16.5	1471
042630.7+243637	17.8 ± 1.5	45.1	18.3	43.2	18.2	1476
Threshold ice abundances			H ₂ O, ML	CO ₂ , ML	CO, ML	
A_{th} H ₂ O	3.2 ± 0.1		3.5			1332
A_{th} CO ₂	4.3 ± 1.0			1.5		1375
A_{th} CO ^c	6.8 ± 1.6				0.6	1424
A_{th} CO ^d	8.1				1.3	1437

^aAbundance ratio for icy species

^bIntegration time, corresponding to the A_V value

^cWhittet et al. (2001)

^dPaper II

to specific time-points of the simulations with the corresponding A_V (see Paper II, for more on this approach).

2.2. Chemical model

2.2.1. Reaction network

Several changes have been introduced into the gas-grain network, which was acquired from Laas, Garrod, Herbst, & Widicus Weaver (2011). The four new gas-phase reactions of Vasyunin & Herbst (2013b) were added. All these reactions involve the methoxy radical CH₃O. Because these authors did not discern between the methoxy radical and its isomer, the hydroxymethyl radical CH₂OH, four complementary reactions were added for the latter species (1-4 in Table 4).

The results of Paper II show that formic acid HCOOH, formaldehyde H₂CO, and formamide NH₂CHO can be overproduced in subsurface mantle conditions with the surface reaction set of Laas et al. (2011), which has been adopted from Garrod et al. (2008). In an attempt to reduce their abundance, grain surface reactions 5-8 in Table 4 have been added to the network. They tend to reduce the production efficiency of HCOOH, H₂CO, and NH₂CHO because alternative outcome is now possible for their reactants.

Reactions 5-7 were assumed to be barrierless. Reaction 8 has an assumed activation barrier

$E_A=2100\text{K}$, estimated from reactions of H₂ with compounds that have a similar structure to HCO. The barrier of the latter reaction is so high that it has little effect on the results of the current cold core model.

Reactions 9-11 were added to more adequately reproduce the chemistry of sulfur oxides, with activation barriers taken from similar gas-phase reactions. Finally, reaction 12 was added to avoid most of chlorine atoms ending up in solid ClO, which is probably unrealistic, given the availability of atomic hydrogen, irradiation, and an aqueous medium on grain surfaces. The activation barriers for four additional surface reactions – 13-16 in Table 4 – were also changed, in line with available data.

2.2.2. Surface and bulk ice chemistry

The rate for reactions on grain surface was calculated according to the reaction-diffusion competition approach of Garrod & Pauly (2011). The modified rate equations method has been applied (see Paper II). As explained in Section 2.1.3, part of surface reaction products desorb into the gas. Reaction barriers are overcome either thermally or by quantum tunneling, whichever is faster (Garrod et al. 2008).

The rate of binary reactions in bulk ice was calculated for reactants that are immobile for most of the time (Papers I and II). It was assumed that

Table 4: Changes in reactions respective to the original network by Laas et al. (2011).

No.	New gas phase reactions ^a	α	β	γ	Reference
1	$\text{CH}_2\text{OH} + \text{H} \longrightarrow \text{CH}_3 + \text{OH}$	1.6E-10	0	0	NIST
2	$\text{CH}_2\text{OH} + \text{O} \longrightarrow \text{H}_2\text{CO} + \text{OH}$	1.5E-10	0	0	NIST
3	$\text{CH}_2\text{OH} + \text{CH}_3 \longrightarrow \text{H}_2\text{CO} + \text{CH}_4$	1.4E-10	0	0	NIST
4	$\text{CH}_2\text{OH} + \text{CH}_3 \longrightarrow \text{C}_2\text{H}_5\text{OH}$	1.0E-15	-3.00	0	Vasyunin & Herbst (2013b) ^b
No.	New surface (ice) reactions	E_A , K	Reference		
5	$\text{H} + \text{HCO} \longrightarrow \text{CO} + \text{H}_2$	0	This work		
6	$\text{OH} + \text{HCO} \longrightarrow \text{CO} + \text{H}_2\text{O}$	0	This work		
7	$\text{NH}_2 + \text{HCO} \longrightarrow \text{CO} + \text{NH}_3$	0	This work		
8	$\text{H}_2 + \text{HCO} \longrightarrow \text{CH}_3\text{O}$	2100 ^c	This work		
9	$\text{OH} + \text{SO} \longrightarrow \text{SO}_2 + \text{H}$	0	Gas phase		
10	$\text{O} + \text{HS} \longrightarrow \text{S} + \text{OH}$	956	Gas phase		
11	$\text{O} + \text{HS} \longrightarrow \text{SO} + \text{H}$	0	Gas phase		
12	$\text{H} + \text{CL} \longrightarrow \text{HCL}$	0	Gas phase		
No.	Changed surface (ice) reactions	E_A , K	Reference		
13	$\text{CO} + \text{O} \longrightarrow \text{CO}_2$	290	Roser et al. (2001)		
14	$\text{O}_2 + \text{H} \longrightarrow \text{O}_2\text{H}$	600	Du et al. (2012)		
15	$\text{H} + \text{H}_2\text{CO} \longrightarrow \text{CH}_3\text{O}$	2100	Woon (2002)		
16	$\text{O}_3 + \text{H} \longrightarrow \text{O}_2 + \text{OH}$	0	Mokrane et al. (2009)		

^aIn addition to the four reactions from Vasyunin & Herbst (2013b). Reaction rate coefficient $k = \alpha(T/300)^\beta \exp(-\gamma/T)$

^bData adopted from $\text{CH}_3\text{O} + \text{CH}_3$ reaction

^cEstimate

each molecule vibrates in a lattice cell with ten neighboring molecules. Reactants have to overcome a certain energy barrier $E_{\text{prox}} = 0.1E_D$ in order to achieve sufficient proximity for a reaction to occur. Molecule diffusion in ice and reaction-diffusion competition have been taken into account in a manner, similar to that for surface reactions. I refer the reader to Papers I and II for a more detailed justification and formalism for the calculation of reaction rate coefficients.

Surface and bulk-ice molecules are subjected to photodissociation by interstellar and cosmic-ray-induced photons. For surface species, the dissociation rate has been taken to be equal to that of gas-phase species. For molecules within the mantle, the photon flux is attenuated by overlying MLs. Each ML has an assumed absorption probability of 0.007 (Andersson & van Dishoeck 2008). In order to calculate the photon flux, respective to each sublayer, the value relevant to middle ML of that sublayer was used (see Paper II).

3. Results: ice formation and major components

To avoid repetition in the studies of five roughly similar models of objects of the same class, the modeling results are not reviewed for each case separately. Instead, we focus on several astrochemical problems, relevant for ices in starless cores. The use of five models with physical conditions derived from observations instead of an abstract model adds to the credibility of the research. We also have to keep in mind that the 0D model adequately represents only the center part of each core. The abundances values used here are calculated with $N(X)/N(\text{H})$, i.e., relative to total hydrogen. This means that observationally detected abundances that are given relative to H_2 were divided by two for comparison with calculation results.

3.1. The evolution of the ice layer

Ice layer is basically nonexistent (around 0.1ML) when $A_V < 1.9\text{mag}$, which means that the calculation results (abundances of species) are irrelevant for ice chemistry if $t \leq 1\text{Myr}$. Because of this, we interpret results for integration times $t > 1\text{Myr}$, only. Ice formation observes the rules outlined in Paper II. As the cloud contracts and

A_V increases over 2mag, ice molecules begin to accumulate on grain surfaces, forming a mixture of H_2O , CO_2 , and NH_3 . The ice is dominated by interstellar photons, which means that all surface CO is oxidized to CO_2 via the sequence:



probably the most important chemical transformation in bulk ice. When the cloud becomes darker, the flux of interstellar photons is diminished, rapid ice photoprocessing becomes impossible, and CO begins to accumulate at $A_V > 5$. The accretion of CO is faster than the surface synthesis of CO_2 , and CO becomes the second most abundant ice molecule when $A_V > 12\text{mag}$.

Figure 2 shows the nominal thickness of ice and the abundances in MLs for a few most important species in each sublayer for all five starless cores. Ice thickness peaks shortly after the end of the core collapse stage, and then slowly decreases. The reason for this decrease is the conversion of simple ice species into more complex ones via photoprocessing. Most importantly, the sequence (4) converts water and carbon monoxide into carbon dioxide. Thus, the number of molecules per grain and the nominal ice thickness are reduced. This can be seen in figure 3. A significant amount of hydrogen is released in the process. H_2 partially accumulates in the mantle when $T < 10\text{K}$. The inner sublayer 3 is the least affected because it has a lower proportion of CO and it is better shielded than the above layers. These results are different from those of Chang & Herbst (2014) thanks to the gradual increase of gas density and A_V during Phase 1, which ensure an ice composition that is much more differentiated between layers. Such a chemical differentiation (H_2O in inner and CO in outer layers) has been confirmed by models that consider ice formation in collapsing cores with monolayer accuracy (Garrod & Pauly 2011; Taquet et al. 2014).

CB 26 is the smallest of the five cores, it has the lowest final A_V and density values (Table 1). This means that molecules on grains deposit at a lower rate, and have undergone significant subsurface photoprocessing even before the freeze-out has ended. With the ‘freeze-out epoch’ we understand the interval between the time of formation for the first sublayer (t_{sub}) and the time, when maximum ice thickness is reached (t_{max} , as speci-

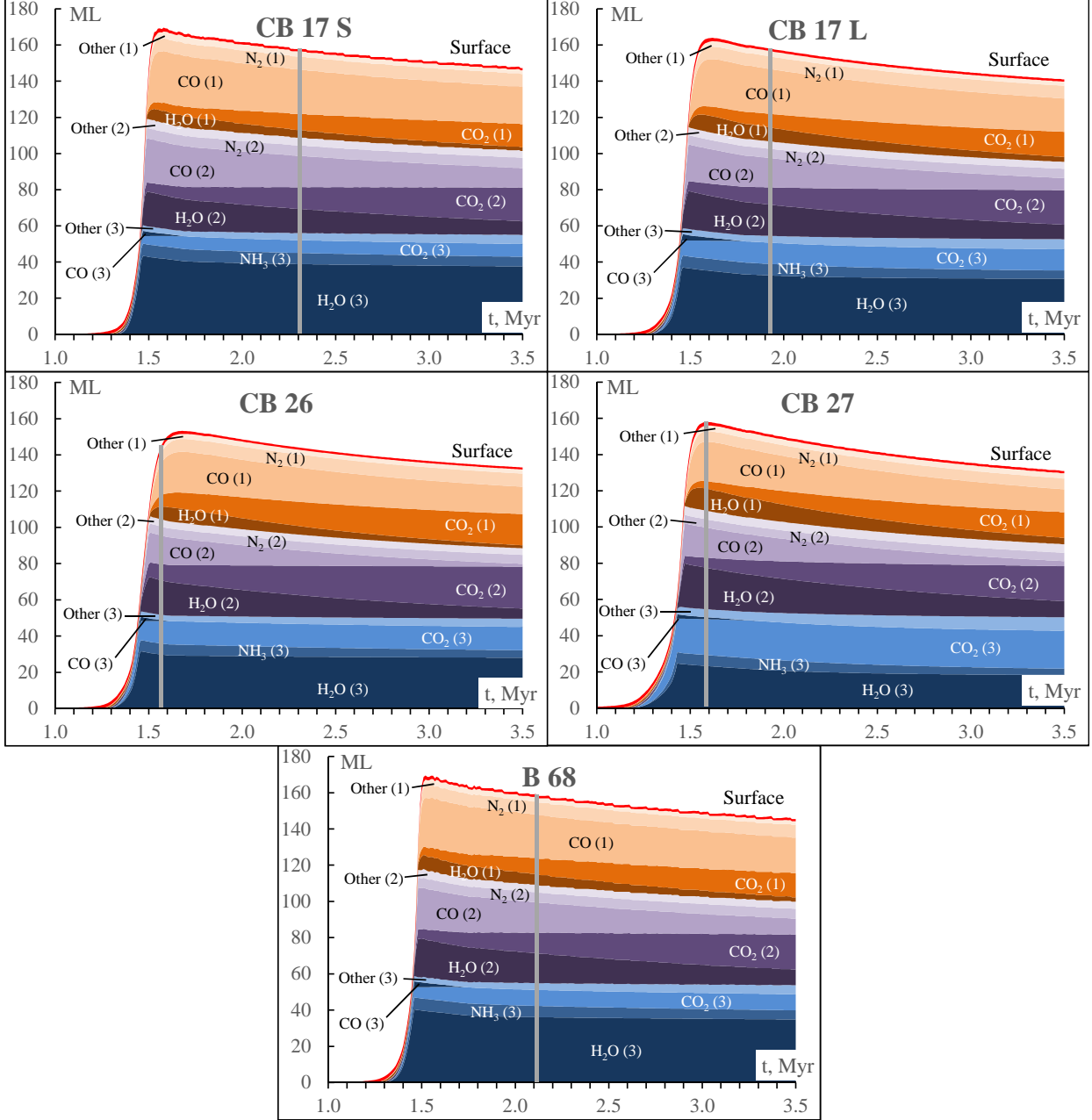


Fig. 2.— Calculated ice thickness and abundance in MLs for major species in the sublayers for the modeled cloud cores. The number in parenthesis indicates the number of the respective sublayer, while ‘Other’ stands for all other icy species in that sublayer. The vertical gray line indicates t_{50} for each model.

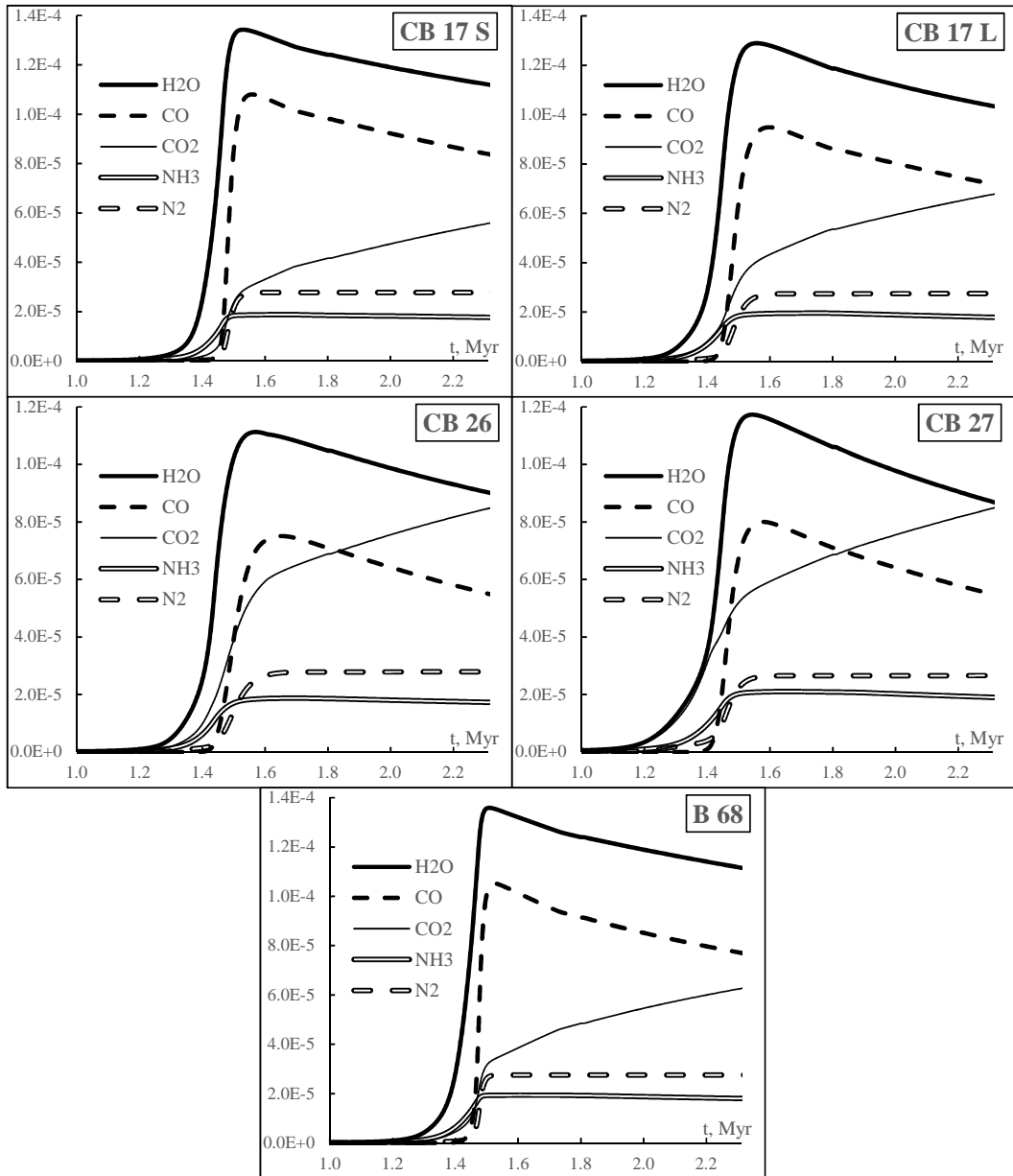


Fig. 3.— Calculated abundances, relative to H atom number density, of major species in ice for the five modeled cores.

Table 5: Calculated ice composition parameters in the starless core models.

Core	A_V	t_{sub} , Myr	Max. ice thickness				t_{50} , Myr	Ice at 3.5Myr		
			ML	t_{max} , Myr	$\frac{\text{CO}}{\text{H}_2\text{O}}$, %	$\frac{\text{CO}_2}{\text{H}_2\text{O}}$, %		ML	$\frac{\text{CO}}{\text{H}_2\text{O}}$, %	$\frac{\text{CO}_2}{\text{H}_2\text{O}}$, %
CB 17 S	13.8	1.25	170	1.57	81	23	2.31	147	68	81
CB 17 L	9.1	1.21	164	1.62	74	35	1.92	141	61	107
CB 26	6.5	1.21	153	1.68	69	59	1.57	133	48	150
CB 27	9.5	1.06	158	1.60	69	51	1.58	131	51	175
B 68	17.6	1.15	171	1.52	78	25	2.12	146	63	90

NOTE.— t_{sub} —time for ice thickness to reach 1ML; t_{max} —time of maximum ice thickness; t_{50} —time for the $\text{CO}_2:\text{H}_2\text{O}$ ice abundance ratio to reach 50%.

fied in table 5). t_{50} is the point in time when the $\text{CO}_2:\text{H}_2\text{O}$ ratio in ice has grown to 50%, and for CB 26 it occurs even before t_{max} .

On the other hand, CB 27 is the largest core considered. Paradoxically, this results in a similar ice composition to that of CB 26. The A_V threshold for accumulation of a significant mass of ice on the grains ($>1\text{ML}$) is close to 1.9mag. This occurs at a density of $\approx 5 \times 10^3 \text{cm}^{-3}$ for CB 27, and in the range $(8 - 9) \times 10^3 \text{cm}^{-3}$ for the other four cores. The result is that the first ice sublayers in CB 27 appear some 150kyr earlier than in other cores. The formation of sublayer 1 in CB 27 is complete some 20kyr earlier than for the other cores. This means that sublayer 1 has formed in a relatively diffuse environment, which is still largely dominated by interstellar photons, where water photodissociation products combine with CO on the surface to produce an ice that contains a large proportion of CO_2 .

Because indirect reactive desorption, which largely governs ice composition, has been calibrated for the B 68 core (section 2.1.4), the explained mechanisms may lead to different results, if $f_{\text{H}_2\text{fd}}$ is different. The important thing is that both, a diffuse medium or early ice formation, may lead to a significantly photoprocessed ice. The first is characteristic for low-mass molecular cloud cores, while the second is more likely for relatively massive cores.

Table 5 summarizes data for each model at two important points in time: when ice thickness is at its maximum, and at the end of the simulation run. The thickest ice layer is attained in CB 17 S and B 68 models. High ice thickness for B 68

can be expected because of its high extinction and final density. For CB 17 S, neither its density, nor extinction are the highest. A thick ice layer for this core arises because N_{out} for this model is 0, which means that interstellar photons are attenuated to a lesser extent and the ice layer begins to form at a later, denser stage of the collapsing core. In turn, ice accumulates rapidly and undergoes less intense photoprocessing, and a smaller number of CO and H_2O molecules are converted to CO_2 . This results in higher nominal ice thickness. This conclusion is supported by the abundance of carbon oxides – a higher proportion of CO_2 means a nominally thinner ice (Table 5).

The above analysis confirms that extinction largely regulates the formation of the ice layer on the grains because A_V determines the number of interstellar photons that reach the grains (Watson & Salpeter 1972). Interstellar extinction also affects the abundance of radical species on surfaces and in the gas, which determines the efficiency of direct and indirect reactive desorption. It can be safely said that the formation history of a starless or prestellar core determines its ice composition.

3.2. General ice chemistry

Aside water and carbon oxides, the nitrogen species NH_3 and N_2 also can be considered major ice constituents. Their abundance is little affected by ice photoprocessing. Other ice species whose abundance may exceed 1% relative to water for at least one of the modeled cores include H_2 , O_2 , H_2O_2 , O_2H , and H_2S .

Figure 2 shows ice evolution up to 3.5Myr,

the full length of the simulation runs. Although the modeled cores have different physical parameters, ice sublayers share a similar composition in all cases. The inner sublayer 3 contains a large amount of water, in addition to CO_2 and NH_3 . All CO molecules here are quickly consumed, which makes chemical processes in sublayer 3 somewhat different to those in above layers. The lack of CO and its daughter atomic C means that O, OH, N, NH, S, and other radicals are more available.

Sublayer 2 initially forms as a $\approx 1:1$ mixture of H_2O and CO, with additions of CO_2 and N_2 . As the time progresses, CO and H_2O combine, and the sublayer becomes increasingly dominated by CO_2 . The outer sublayer 1 largely consists of CO, with an admixture of H_2O , CO_2 , and N_2 at roughly similar proportions. CO remains the main species in this layer, although the proportion of CO_2 is steadily growing. Sublayer composition may profoundly affect the chemistry of minor species because the main reacting species are photodissociation fragments of major molecules.

3.3. Comparison with observations and age limits

The initial chemical composition of ices is largely regulated by indirect reactive desorption, calibrated with the B 68 model (section 2.1.4). Table 3 shows that carbon oxides are somewhat depleted during the earlier stages in cloud contraction, compared to the observational data by Whittet et al. (2007). We found it impossible to remove this discrepancy with adjustments in the efficiency of indirect reactive desorption, Equation (3). This depletion may arise, for example, if the calculated abundance of atomic H is higher by a factor of two than H abundance in the real core. Another possible cause can be changes in surface properties as proportionally more and more CO molecules stick to the grains during the ice formation epoch. We will investigate the latter suggestion in a separate paper.

Figure 4 shows that molecules, typically formed on grain surfaces or dense gas (e.g., H_2O , CO_2 , NH_3 , and O_2), are also abundant in the gas phase during or immediately after the core contraction stage, when density is in excess of $\approx 10^4 \text{cm}^{-3}$. Gas and surface molecules are actively interchanged during the freeze-out epoch. Such gas-phase abundance peaks in a layer around a collaps-

ing core have been found in models of prestellar cores (Garrod & Herbst 2006; Vasyunin & Herbst 2013a, ; Paper II) and observations of water vapor in the prestellar core L1544 (Caselli et al. 2012). The present model predicts is that such peaks are likely to be shorter and higher thanks to more efficient desorption mechanisms. Desorption retains a substantial amount of refractory species in the gas phase until very late times in core contraction.

We can conclude that the Phase 1 modeling results confirm that gas falling into a prestellar or protostellar core is rich with molecules synthesized on the surface. The abundance peaks predicted by the present study are higher than in other similar models, thanks to more efficient desorption mechanisms. The main desorption agent are interstellar photons, as suggested by Dominik et al. (2005).

Subsurface ice processing may place constraints for the maximum age of starless cores. The observed solid $\text{CO}_2:\text{H}_2\text{O}$ abundance ratio does not exceed 44% (Boogert et al. 2011), although higher values are permitted by upper limits. As a threshold value for the age of the cores we chose the longest time taken for any of the cores to reach a $\text{CO}_2:\text{H}_2\text{O}$ ice abundance ratio of 50%, corresponding to a time t_{50} . For the CB 17 S core $t_{50} = 2.31 \text{Myr}$, longer than t_{50} for other cores (Table 5). A single end time of 2.31Myr was applied for all simulations. The decision to adopt a single and rather long total integration time for all models results in that for the CB 26 and CB 27 cores $\text{CO}_2:\text{H}_2\text{O}$ is higher than 50% for most of the time. With this approach the model considers a variety of icy environments and allows for an easy comparison between the five simulation results.

The above means that the actual lifetime t_2 of a quiescent Phase 2 core with constant physical conditions is below 0.9Myr for all models. This is significantly less than the initial assumption of $t_2 \approx 2 \text{Myr}$ for a 3.5Myr total simulation length. Thus, the modeling results were analyzed for an integration time interval of 1.00-2.31Myr.

If gas and dust in the center part of a starless core is not effectively mixed with its surroundings, CO_2 -rich ices should be present in starless cores. Turbulence and mixing of gas in the dense cores is a poorly-known parameter that may contribute to the destruction of the ices (Boland & de Jong 1982; Williams & Hartquist 1984; Redman et al. 2006; Adams & Shu 2007; Levshakov et al. 2014;

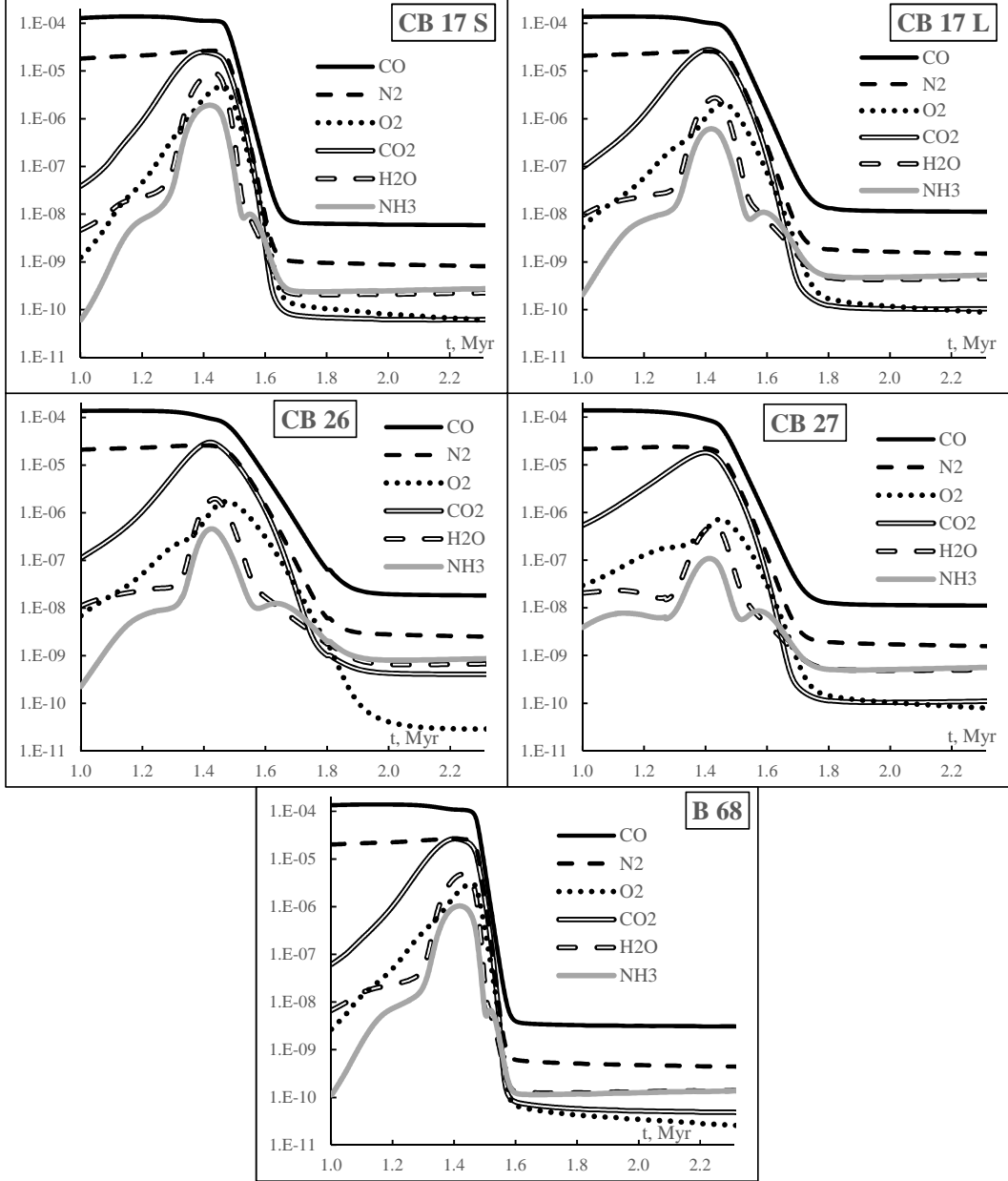


Fig. 4.— Calculated abundance of major gas phase molecules, relative to hydrogen.

Steinacker et al. 2014). Given the uncertainties, we treat the chemistry of CO₂-rich ices as a theoretical possibility. Their observational detection or non-detection might provide additional constraints on the physico-chemical processes that govern ice formation, chemical processing, and desorption.

4. Results: elemental chemistry

4.1. Oxygen chemistry in ice

4.1.1. Chemical processing of minor oxygen species

Three major ice species – H₂O, CO, and CO₂ – contain copious amounts of the eighth element, and the chemistry of oxygen in ice is closely connected to these molecules. When water and carbon oxides are excluded, the bulk ice chemistry of oxygen for CB 17 S and B 68 is initially dominated by molecular oxygen O₂, which is rather quickly converted into hydrogen peroxide H₂O₂, as shown in figure 5. For other models, where ice photoprocessing is more intense, H₂O₂ is the more important species from the beginning. H₂O₂ is more stable in irradiated interstellar ices than O₂, which mainly arrives from the gas phase. The hydroperoxyl radical O₂H is the most abundant radical for oxygen chemistry in ice, thanks to its high E_b , M . It is generated by two mechanisms – H addition to O₂ (early times) and the photodissociation of H₂O₂ (late times). Hydroxyl radical OH begins to accumulate to a limited extent in the inner sublayer 3 only after the CO molecule has been oxidized.

Interestingly, CB 26, which has the lowest A_V and highest flux of interstellar photons, has also the lowest radical content. This is because the higher temperature in CB 26 (see Table 1) allows a greater radical mobility (especially for atomic H) in the mantle and, thence, reactivity. Low radical content in CB 26 ices is characteristic also for other compound classes (sections 4.2, 4.3, 5.1).

Because ice in CB 17 S is initially rich in O₂ (figure 5), it has also a higher abundance for H₂O₂, which forms via reaction 14 (Table 4). Substantial amounts of H₂O₂ (relative abundance $X_{\text{H}_2\text{O}_2}$ in excess of 10⁻⁶) in sublayer 3 for CB 17 S and B 68 are able to form from water photodissociation products that combine together after all CO

has been oxidized in that sublayer.

4.1.2. Comparison with observations

Figure 7 shows that the calculated abundance of gaseous hydrogen peroxide H₂O₂ can be reasonably high for a short period, up to 9×10^{-10} relative to total hydrogen atomic number density for CB 17 S. The abundance of its associated O₂H radical, however, is lower by three orders of magnitude. Both these species have been observed in interstellar medium with roughly similar abundances of 5×10^{-11} (Bergman et al. 2011; Parise et al. 2012). It has been suggested that reactive desorption is responsible for transferring these species from the surface to the gas (Du et al. 2012). However, reactive desorption may be too inefficient to maintain a significant amount of such heavy species in the gas (Paper II). The comparison of abundances here is indicative, only, because of the limits of the 0D model.

Because practically all of H₂O₂ in ice resides in the sublayers, photodesorption from subsurface ice may play a role in the existence of gas-phase H₂O₂ and O₂H. More often than not, dissociative photodesorption occurs, when molecule fragments are ejected, instead of intact species (Andersson et al. 2006; Andersson & van Dishoeck 2008). This aspect has not been considered in the present model, or in the model by Du et al. (2012). It likely that photodesorption of H₂O₂ also induces a high gas-phase abundance of O₂H.

Beginning with Goldsmith et al. (2002), molecular oxygen O₂ has been repeatedly observed in shocked gas. A few detections have been associated with the cold dense core ρ Ophiuchi A, with inferred abundances in the range $2.5 \times 10^{-7} \dots 1.25 \times 10^{-6}$ relative to total hydrogen. Such a high abundances likely can be observed only during a short period in the core’s evolution (Larsson et al. 2007; Liseau et al. 2010). These results agree with the calculation results shown in figure 7, where the maximum abundances lie in the range $7 \times 10^{-7} \dots 4.5 \times 10^{-6}$. A quantitative comparison is possible in this particular case because of the centrally localized nature of the observed source (Liseau et al. 2010).

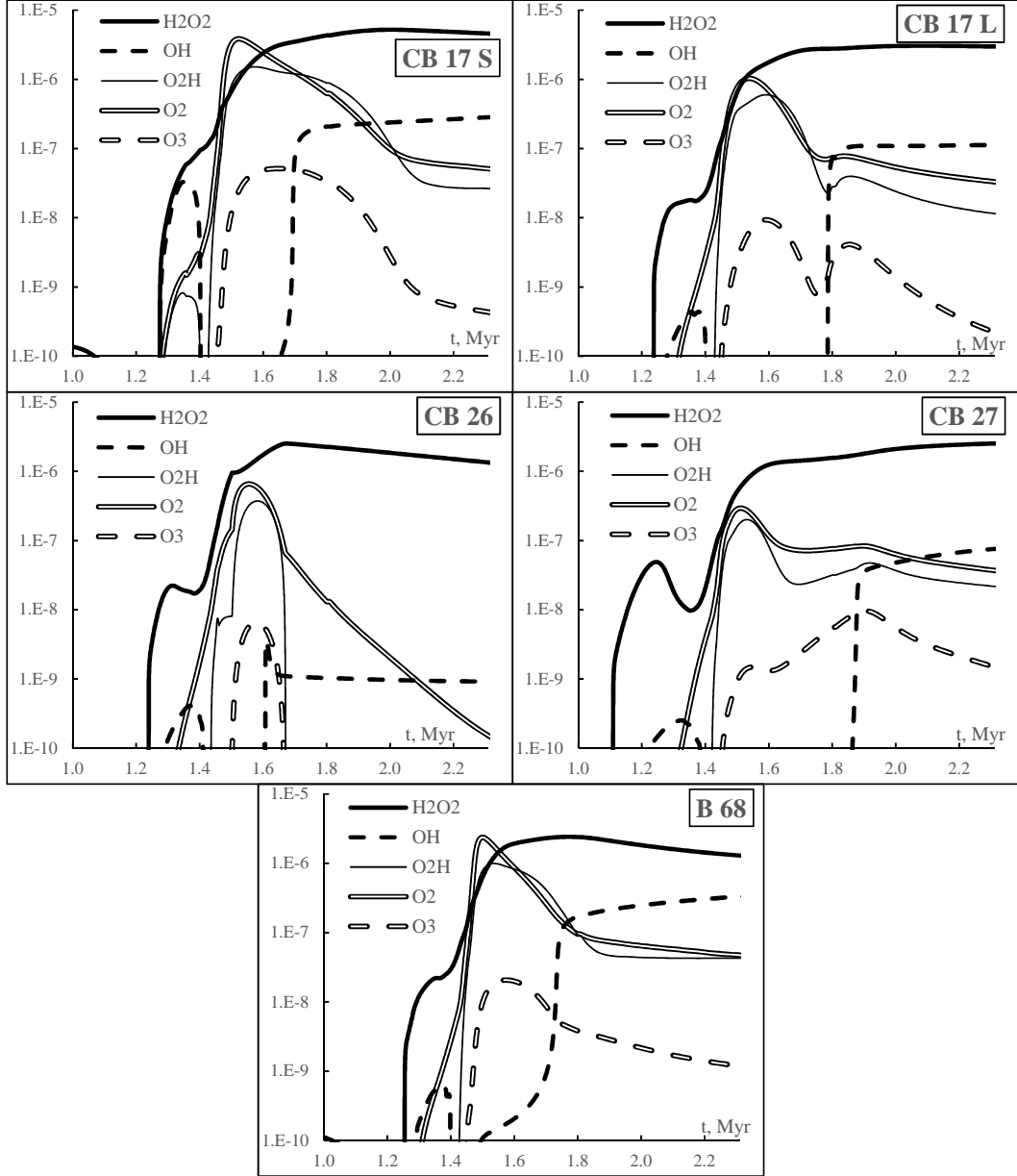


Fig. 5.— Calculated abundance of selected oxygen species in ice, relative to hydrogen.

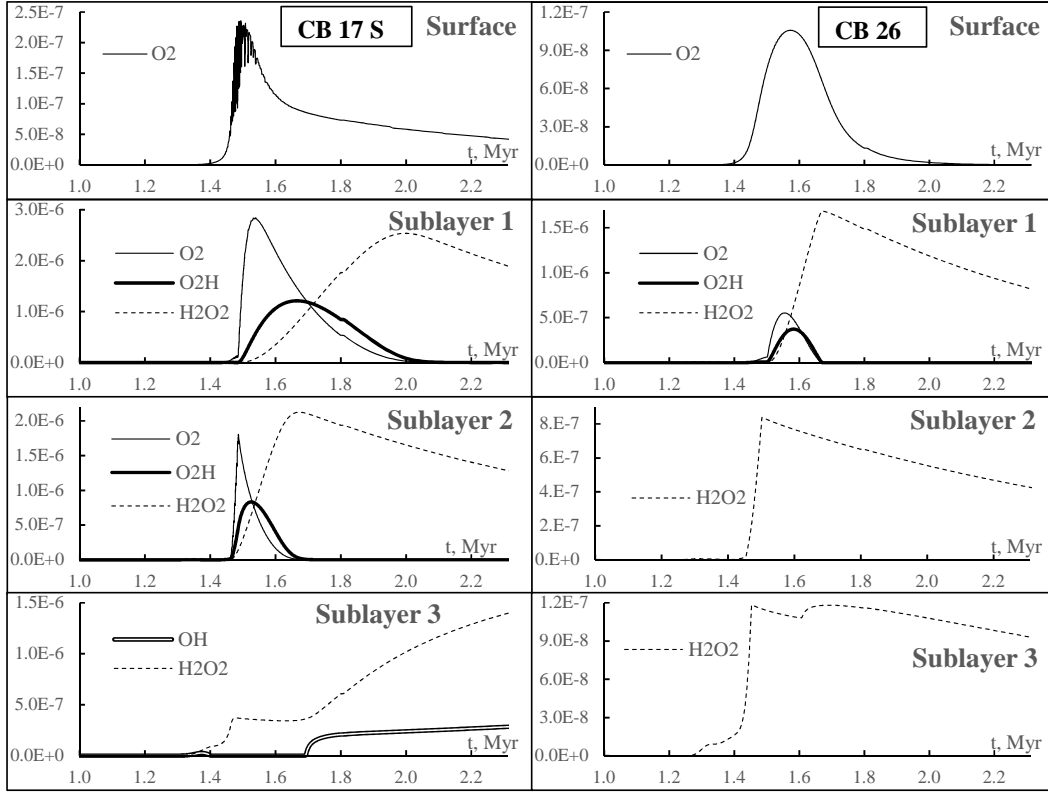


Fig. 6.— Calculated relative abundance of main O and O-H species in ice mantle sublayers for CB 17 S, and CB 26 models. The latter represents a significantly photoprocessed ice. The irregularities for CB 17 S surface layer at $t \approx 1.5$ Myr are artifacts.

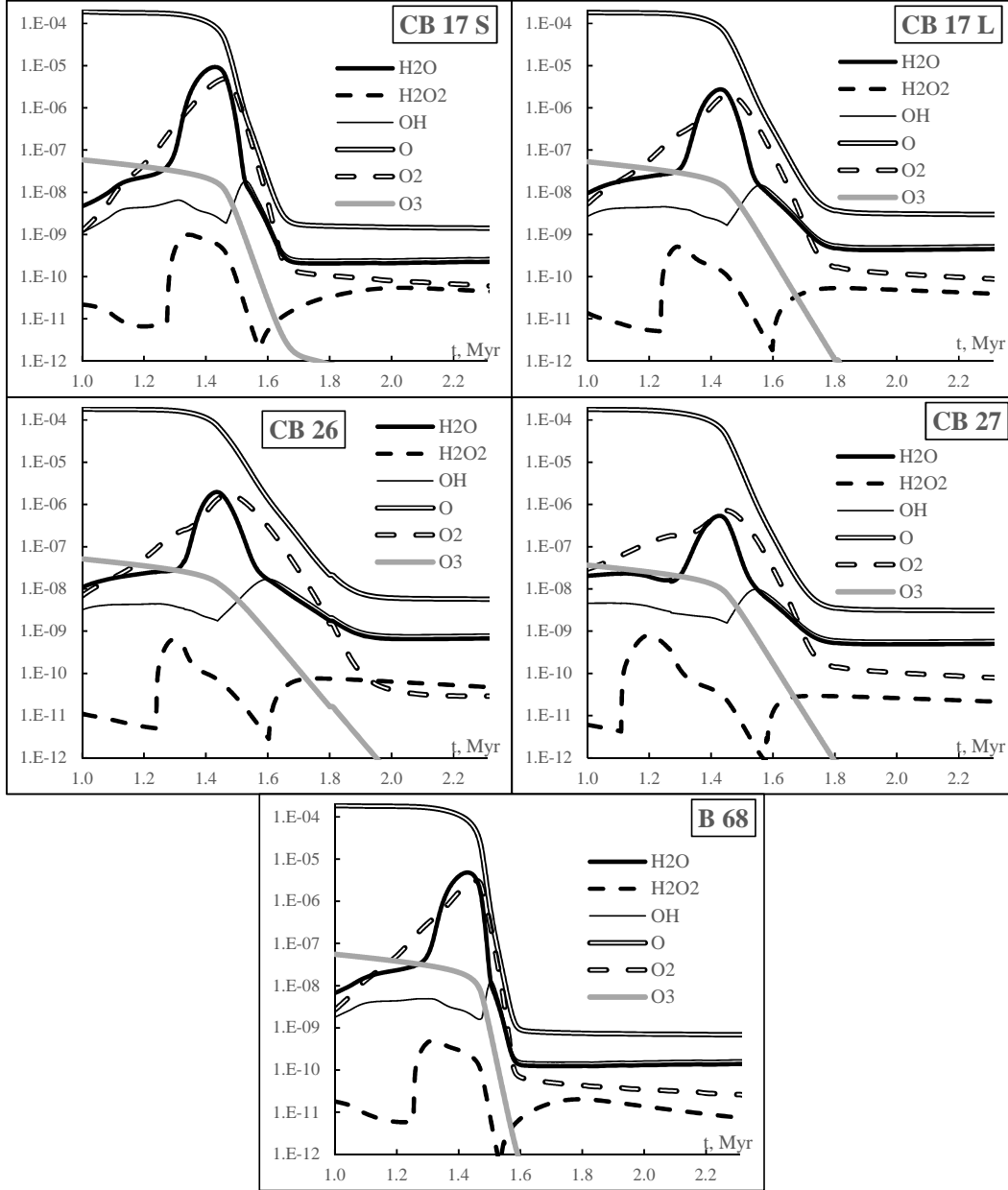


Fig. 7.— Calculated abundance of selected oxygen species in gas phase, relative to hydrogen.

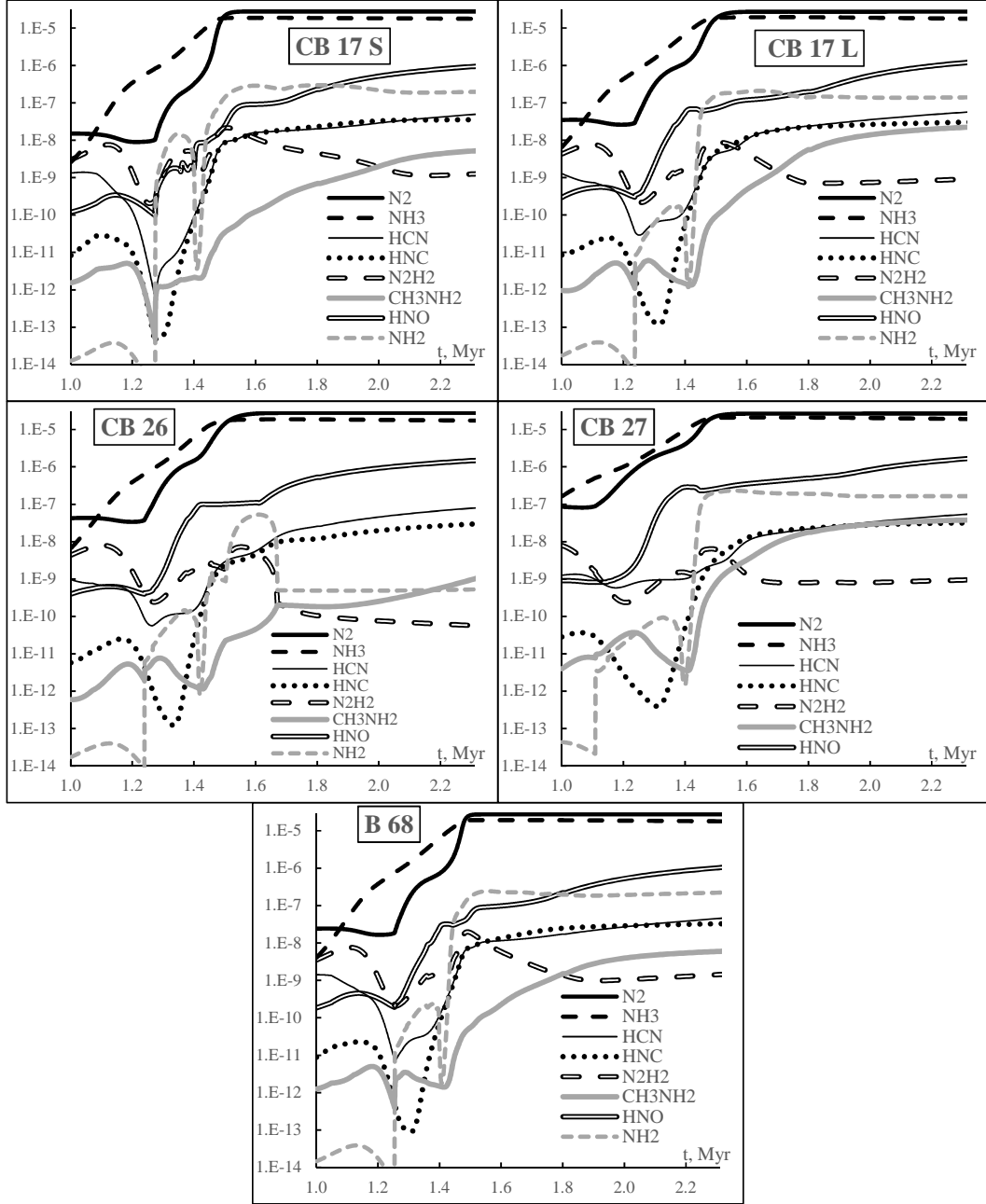


Fig. 8.— Calculated abundance for important nitrogen species in ice, relative to hydrogen.

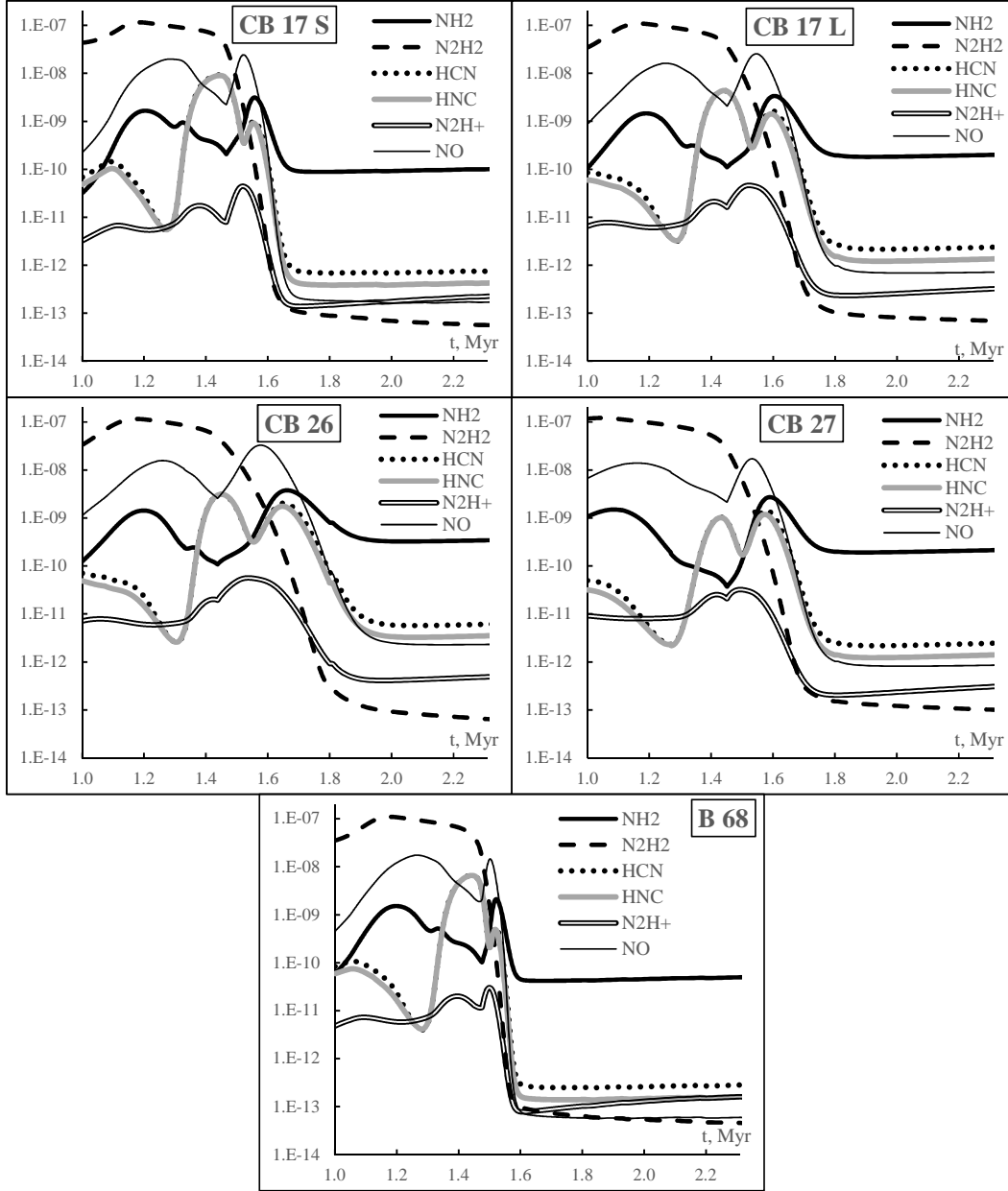


Fig. 9.— Calculated abundance of important nitrogen species in gas phase, relative to hydrogen.

4.2. Nitrogen chemistry in ice

4.2.1. Chemistry of important species

Figures 8 and 9 show that ammonia NH_3 and molecular nitrogen N_2 are the main nitrogen reservoirs in ice and gas. Nitrogen chemistry is regulated by proportions of N_2 and NH_3 in the surface and the three sublayers (section 3.2). The relatively clear division of NH_3 (in sublayer 3) and N_2 (in sublayers 1 and 2) means that N , NH , and NH_2 radicals are not equally available in all sublayers. Interesting examples of relatively abundant minor nitrogen species in ice are formamide NH_2CHO (discussed in section 5), hydrogen cyanide HCN and isocyanide HNC .

The chemistry of HCN and HNC is controlled by the proportions of CO , N_2 , and NH_3 in each sublayer. HNC is more favored by ice chemistry at earlier times than cyanide HCN , while HCN is the more favored isomer during late times. The two isomers form via different pathways. HNC is mainly synthesized in the reaction $\text{NH}_2 + \text{C}$, while HCN is the product of H addition to CN . The latter forms via $\text{C} + \text{N}$. This means that HNC is a product of NH_3 and CO mixture photoprocessing, while HCN is synthesized in a N_2 and CO mixture. The HNC pathway is more efficient because it requires no subsequent hydrogenation. The result is that 60 (for CB 17 S) to 90% (for CB 26) of both isomers are concentrated in the outer sublayer 1, where CO and N_2 are highly abundant, and NH_3 is available, too. The remaining 10-40% reside in sublayer 2, while sublayer 3 is very poor on HCN and HNC (<2%), because of a lack of CO there. Because the surface closely interacts with gas-phase CO and N_2 , HCN is the main isomer for the top ice layer.

4.2.2. Comparison with observations

Recent observed NH_3 gas-phase abundances, lie in the range 9×10^{-9} ... 7.5×10^{-8} relative to total H (Ruuskanen et al. 2011; Levshakov et al. 2014). Crapsi et al. (2007) derives a central NH_3 abundance of 4.5×10^{-9} for the L 1544 dense core. These values qualitatively agree with calculation results for cores with ages in the range $t = 1.5$... 1.8 Myr.

Figure 10 shows the calculated $\text{HNC}:\text{HCN}$ abundance ratio the center of the respective dark

cores in gas and solid phases. We note that the observed gas-phase values of this ratio are in the range of 0.54-4.5, with no distinction between YSOs and starless cores (Hirota et al. 1998). $\text{HNC}:\text{HCN}$ ratio in ice may exceed unity for all cores, except for CB 26, where lower abundance of CO prevents the build-up of HNC . The highest calculated $\text{HNC}:\text{HCN}$ ratio is in CB 27 ice phase, where it reaches 1.75 briefly at 1.54 Myr. Such a peak arises because of effective HNC production in sublayer 1, not observed in other simulations. In turn, this occurs because sublayer 1 in CB 27 is richer in NH_3 by a factor of >2 than in other models. Finally, NH_3 is more abundant because ices in CB 27 are accumulated at lower extinctions, which means a higher proportion of species that form from free atoms on the surface (H_2O , NH_3 , CH_4 , etc.).

4.3. Sulfur chemistry in ice

Figures 11 and 12 show that H_2S and SO are the most abundant sulfur species in ice and gas. H_2S is more abundant than SO for most of the time. An exception is the CB 26 core, where H_2S is the only dominant species and SO ice forms with a maximum relative abundance of 5×10^{-8} at 1.56 Myr, only, thanks to surface reactions. Then, SO is quickly consumed by ice mantle reactions because of the higher temperature in the CB 26 core. In the other four cores, the HS radical accumulates and has time to react with atomic O , producing SO . Increased mobility of hydrogen in CB 26 ice does not allow the accumulation of HS , S , and many other radicals. H_2S can be expected to be the main sulfur reservoir for photon-dominated ices. Notably, CB 26 still has a maximum SO gas-phase abundance comparable to that in other modeled cores (figure 12).

The abundances of minor sulfur molecules are affected by the proportions of major ice constituents. Molecules, whose synthesis is associated with CO and its daughter radicals (primarily atomic C , atomic O is available also from CO_2), include OCS , CS , H_2CS , and C_2S . These are primarily associated with sublayers 1 and 2 (see figure 13). Oxidized forms SO_2 and NS arise in sublayer 3. The above is true for cores CB 17 L, CB 17 S, CB 27, and B 68. For CB 26, the diversity is largely limited by the dominating H_2S . The efficient synthesis on the surface and subse-

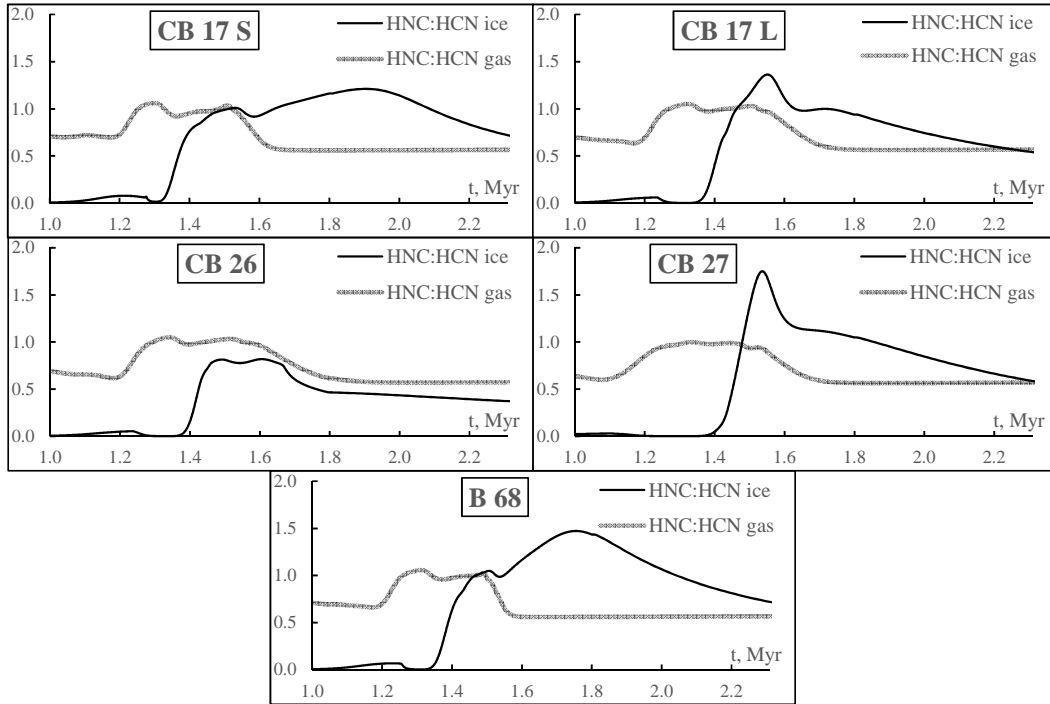


Fig. 10.— Calculated HNC:HCN abundance ratio in gas and ice.

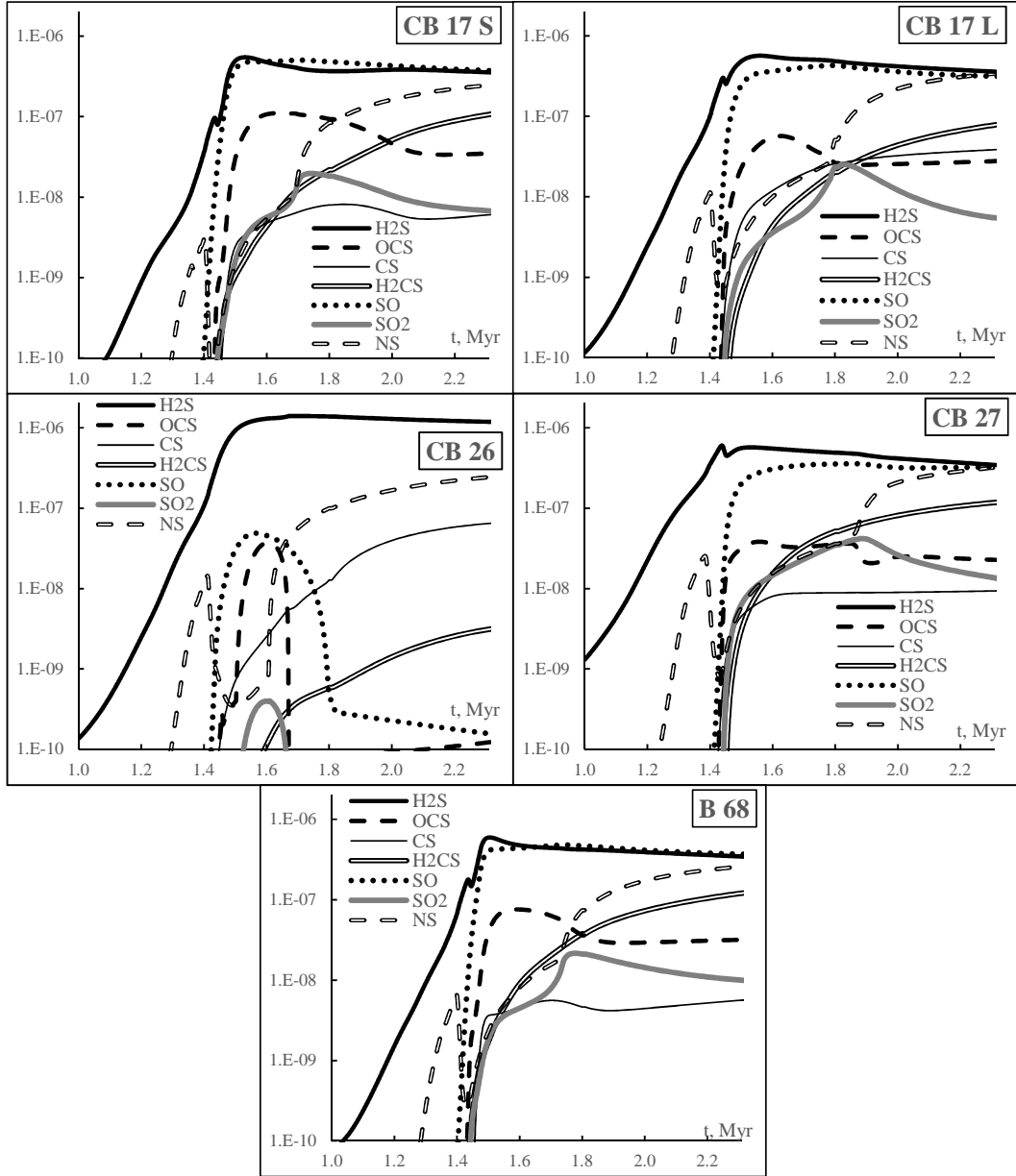


Fig. 11.— Calculated abundance of important sulfur species in ice, relative to hydrogen.

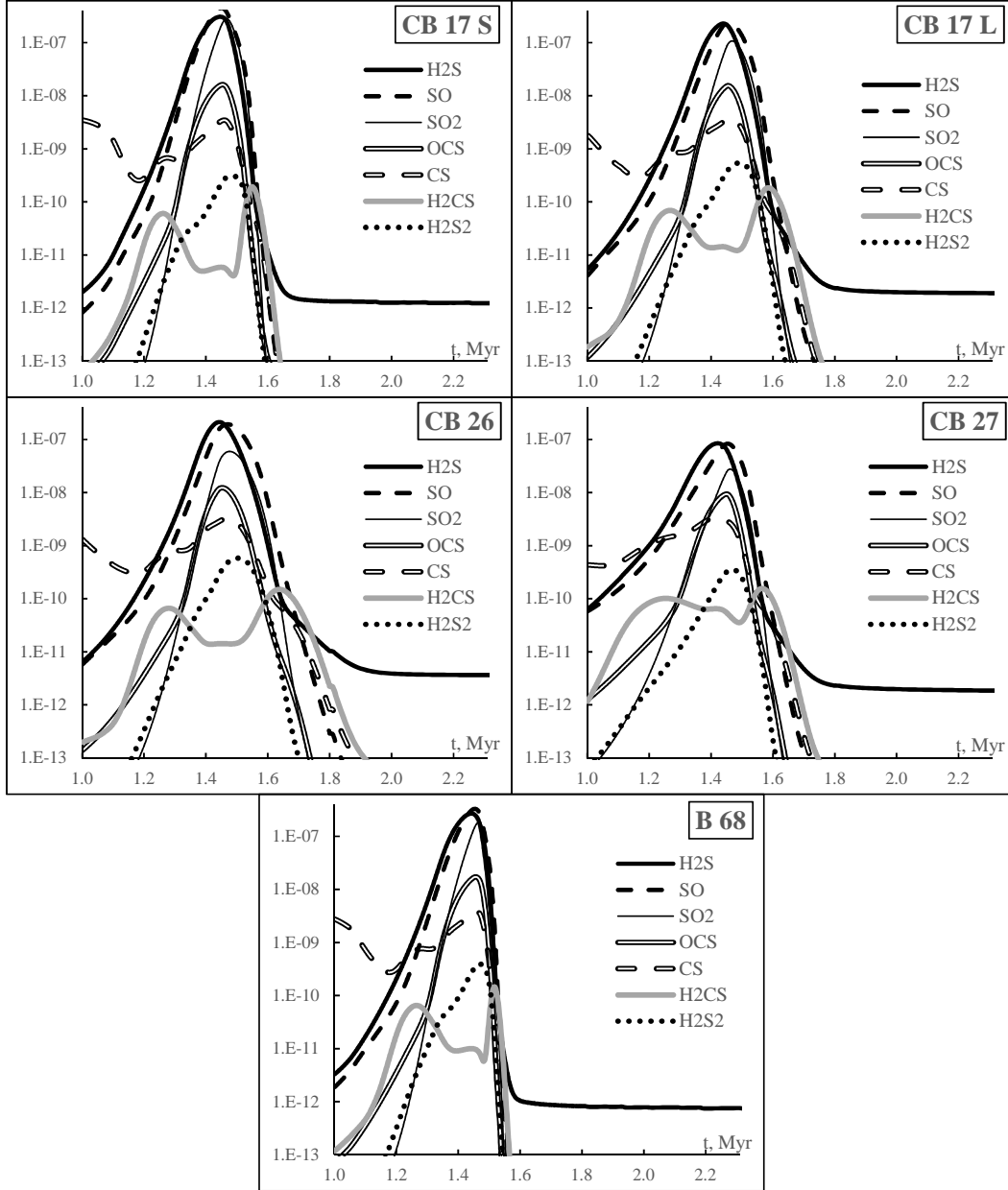


Fig. 12.— Calculated abundance of important sulfur species in gas phase, relative to hydrogen.

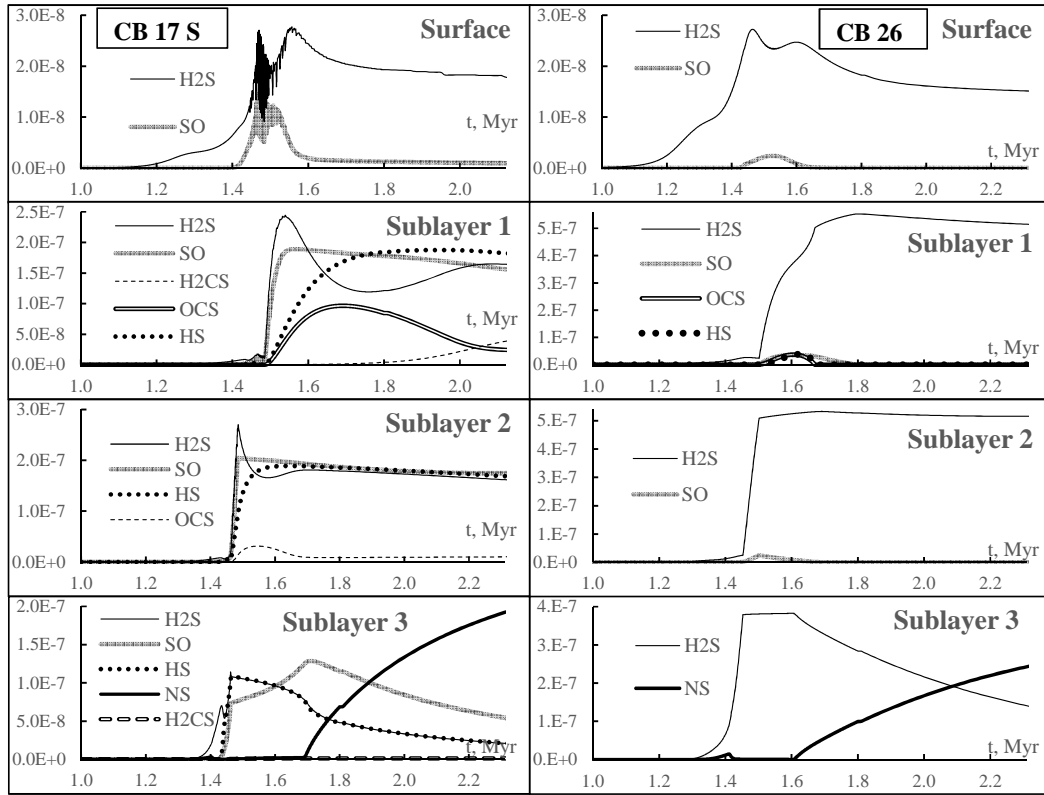


Fig. 13.— Calculated abundance, relative to hydrogen, of main sulfur species in ice mantle sublayers for CB 17 S and CB 26. The latter represents an significantly photoprocessed ice.

quent reactive desorption explain why H_2S is the most abundant sulfur gas phase molecule for all modeled cases.

Modeling results show that H_2S and SO ices are produced during the freeze out epoch and contain most of the sulfur reservoir in interstellar ices. The reaction set for sulfur species is rather poor and does not include sulfurous and sulfuric acids (H_2SO_3 and H_2SO_4 , respectively) that likely are very stable forms of sulfur in watery environment. Oxoacids and their derivatives are possible and non-detectable forms of sulfur in star-formation regions (Kalvāns & Shmied 2010). Given the rich chemistry of sulfur and the radical nature of the SO molecule, it is unlikely that SO is a final, stable, and abundant form of S in interstellar or circumstellar ices. More likely, in terms of this model, it can be viewed as a representation of oxidized sulfur (see also Scappini et al. 2003).

Figure 13 shows an example of depth-dependent composition for sulfur species. H_2S and SO are dominant at all depths, except for sublayer 3 at late times, where the abundance of NS is highly enhanced. Although this is probably because of the limited reaction network for sulfur, this illustrates the oxidation of S during longer timescales. Oxidation products are SO , SO_2 , NS or perhaps, other species, not included in the network. Sulfur in the outer sublayer 1 is less susceptible to oxidation thanks to a higher availability of atomic H.

The high abundance of NS in sublayer 3 for CB 17 L, CB 17 S, CB 27, and B 68 is an example how local conditions in the ice mantle may give rise to peculiar chemical features. NS is produced in all layers via the reactions $\text{N} + \text{S}$ and $\text{NH} + \text{S}$. In sublayers 1 and 2 it is also efficiently destroyed via reactions with atomic C and N. Sublayer 3 is poor with CO and N_2 . Thus, C and N are unavailable, and NS accumulates after all remaining CO has been converted into CO_2 .

5. Results: complex organic molecules

When compared to observational evidence, the synthesis of organic species in the model can be characterized as moderately efficient. For some species, gas phase abundances are in temporal qualitative agreement with the observations, for others even ice abundances are well below expec-

tations. To improve this situation, we introduce two simple changes in the model – a modification to CO and H_2CO hydrogenation activation energies and, subsequently, a mild and short temperature spike during the quiescent phase. The results of the three simulations are described in the following sections.

To provide an indication of the observed abundances of gas-phase COMs relative to the calculated values, the observed values have been marked in their corresponding figure panels. The observed values have no temporal or spatial constraints with regard of the present model. The 0D character of the simulation means that a qualitative comparison is possible, only. We assume that the synthesis of an organic molecule is reproduced with a degree of success, if its calculated ice abundance is not lower than its observed gas-phase abundance.

5.1. COMs: Standard model

5.1.1. The chemistry of COMs

The "Standard" model here is the one described in full in section 2. Figures 14 and 15 show the calculated abundances in the center of the starless cores, along with known observational values. The species can be categorized in several overlapping groups:

- those synthesized via the HCO radical, e.g., formic acid HCOOH , formaldehyde H_2CO , methyl formate HCOOCH_3 , formamide NH_2CHO , and acetaldehyde CH_3CHO ;
- those synthesized via the CH_3O radical, e.g., methanol; CH_3OH , dimethyl ether CH_3OCH_3 , HCOOCH_3 , and as a subgroup, species whose synthesis involves CH_3 , which is a daughter of methanol. This subgroup includes CH_3CHO , acetonitrile CH_3CN , and methane CH_4 ;
- carbon chain molecules, e.g., CH_3CHO , propynone CH_2CCO , ketene CH_2CO , and acetylene C_2H_2 ;
- species that are typically formed via atom addition on the surface, e.g., CH_4 , H_2CO , HCO , HCOOH , CH_2CCO , CH_2CO , C_2H_2 , methyl imine CH_2NH , cyanamide NH_2CN , and CH_3CN . A relatively high gas-phase

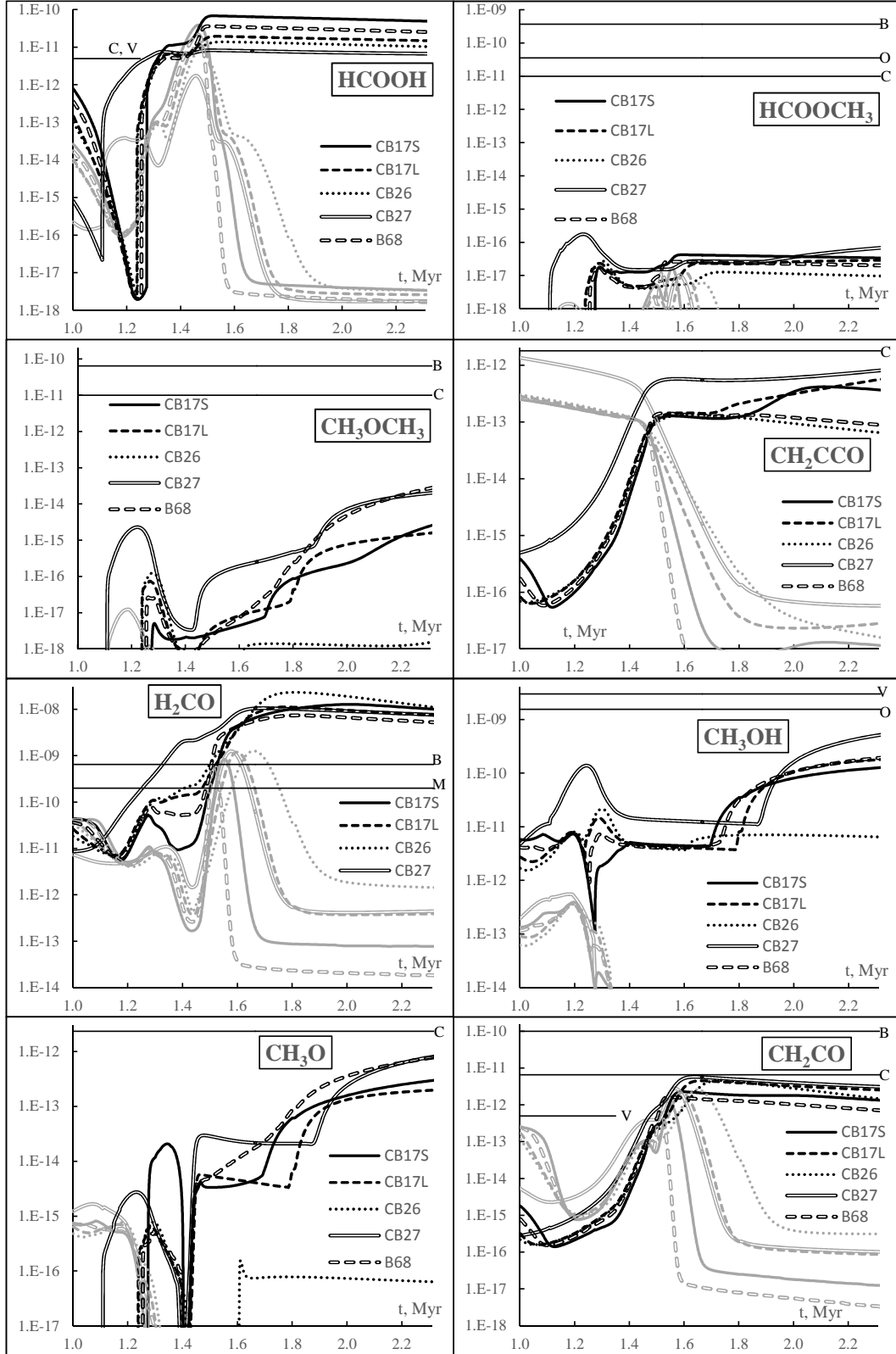


Fig. 14.— Calculated abundances, relative to hydrogen, of observed organic molecules, set No. 1. Gray lines: gas-phase abundance; black lines: abundance in ice (surface and three mantle sublayers). Contraction (Phase 1) ends and the stable core Phase 2 begins at times between 1.4 and 1.5 Myr for all simulations. References: M – Marcelino et al. (2005); O – Öberg et al. (2010); B – Bacmann et al. (2012); C – Cernicharo et al. (2012); V – Vastel et al. (2014).

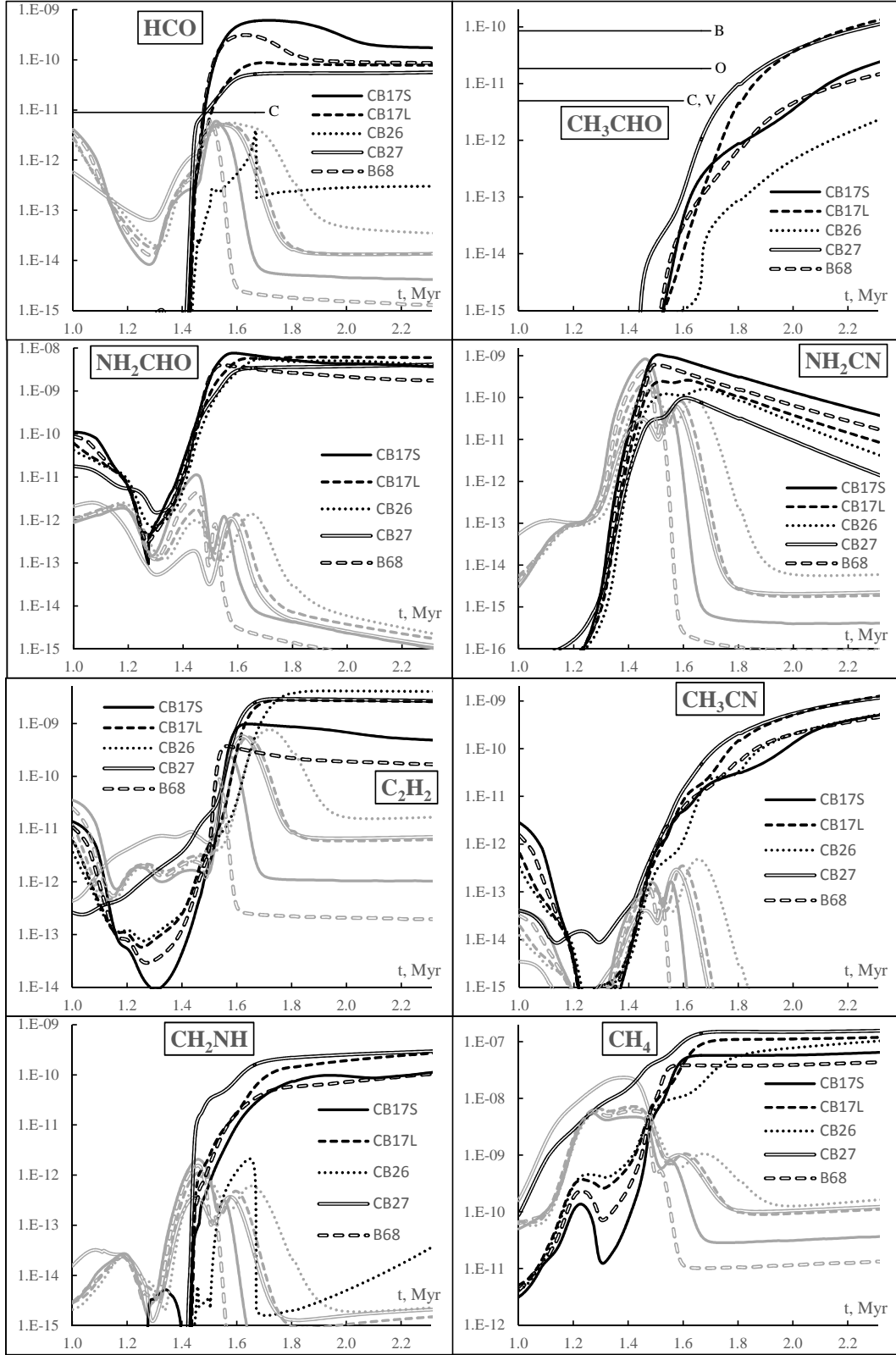


Fig. 15.— Calculated abundances, relative to H, of observed and other selected organic molecules, set No. 2. References as in figure 14.

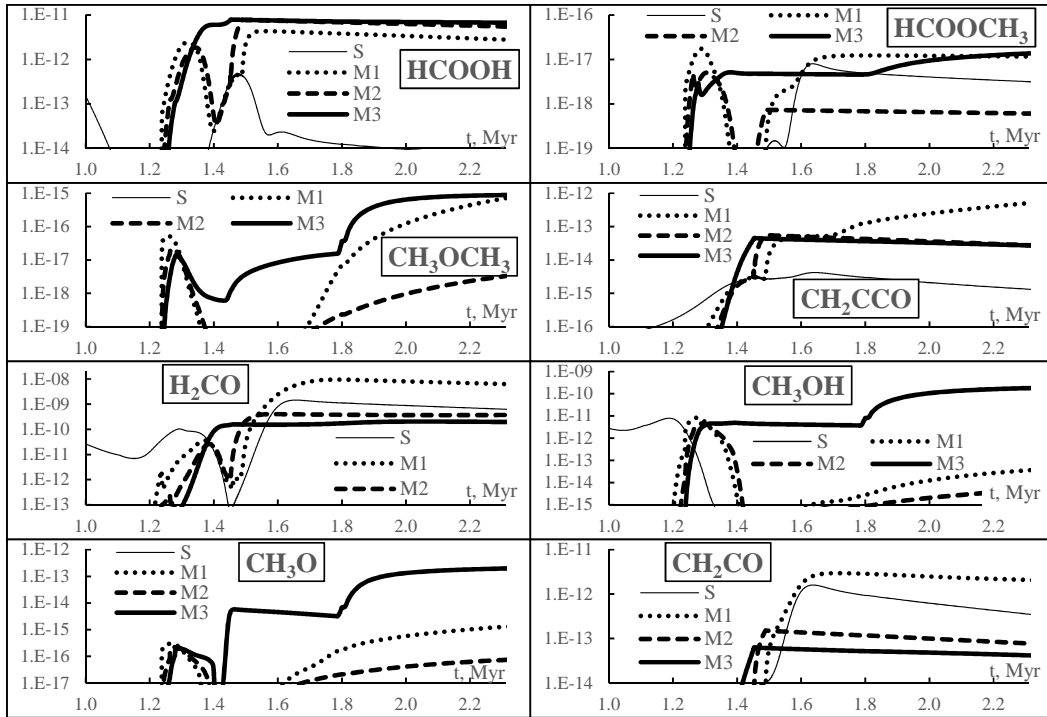


Fig. 16.— Calculated abundances, relative to H, in ice sublayers for selected organic molecules for the CB 17 L core, set No. 1.

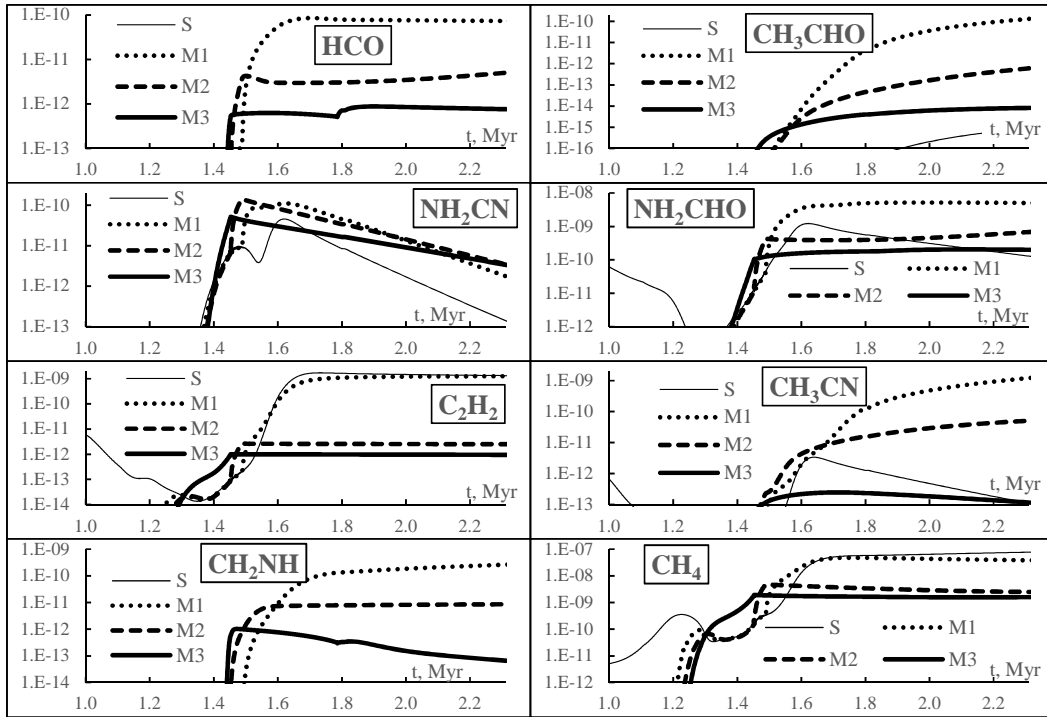


Fig. 17.— Calculated abundances, relative to H, in ice sublayers for selected organic molecules for the CB 17 L core, set No. 2.

abundance during the freeze-out epoch is characteristic for these species.

The hydrogenation of CO and H₂CO are the two most important steps that regulate the general production efficiency for many oxygen-containing COMs in bulk ice. Figures 16 and 17 show the relative abundances of organic species in the four ice layers considered in the models for CB 17 L. This core can be regarded as a ‘median’ case among the five models, without the extremes in ice composition shown by CB 17 S and B 68 on one hand, and CB 26 and CB 27 on the other hand (section 3.1).

Most of the species with abundances shown in figures 16 and 17 have their peak abundances highest in the outermost sublayer 1. This indicates that even a partial ice sublimation might be sufficient to reproduce the observed gas-phase abundances of many COMs. In sublayer 1, CO is available in vast quantities at any integration time points, while the necessary H atoms are produced in H₂O or H₂ photodissociation. With the present 0D model it is not possible to determine the percentage of ice mass that should be sublimated. If the modeled ices are assumed to be representative, this proportion would be $\approx 1 - 10\%$.

5.1.2. Comparison with observations

Figures 14 and 15 show that the model predicts relatively high gas-phase abundance for some species in the HCO group – formic acid HCOOH, formaldehyde H₂CO, and formamide NH₂CHO. Although the observed gas-phase abundances are reached for a short period of time, this occurs during the infall Phase 1 and likely cannot be treated as an agreement with observations of stable starless cores.

For the CH₃O group, the calculated abundances are significantly lower than those observed in interstellar conditions. Even assuming instant ice sublimation, observed gas-phase abundances cannot be reproduced for methyl formate HCOOCH₃, dimethyl ether CH₃OCH₃, and methanol CH₃OH. This result is similar to that of earlier prestellar core models without (Garrod & Herbst 2006; Garrod et al. 2008) and with bulk ice photochemistry (Garrod 2013, Paper II). It is this discrepancy that prompts us to proceed with a more detailed investigation on the chemistry of COMs.

5.2. The Compromise model

5.2.1. Changes relative to the Standard model

In the present surface reaction network (Garrod et al. 2008) the activation energy barriers E_A for reactions H+CO and H+H₂CO are higher than 2000K, which means that they are inefficient for cold core conditions. Experimental evidence points to much lower values for E_A , 300-600K (Awad et al. 2005; Fuchs et al. 2009). However, putting such low E_A values into the present model results in that almost all carbon in ice is in the form of methanol, which is unrealistic. Higher E_A is especially required for the CO+H reaction.

We present results of model calculations that use the experimental, low E_A value for formaldehyde hydrogenation. For CO hydrogenation E_A , an empirical compromise value was used, which lies between the low experimentally detected E_A of Fuchs et al. (2009) and the high (2500K) value proposed by Garrod et al. (2008). Activation energies for the three important CO hydrogenation reactions have been summarized in Table 6. We dub this the “Compromise model” for further reference.

5.2.2. Comparison with observations

Figure 18 shows species, whose abundance is substantially affected with the changes in activation energies for reactions 17, 18, and 19 in Table 6. Comparison with the Standard model results (figures 14 and 15) reveals that the ice abundance of species that are formed via CH₃O is increased by up to six orders of magnitude (CH₃OCH₃ in B 68). Importantly, the ice abundances of CH₃OCH₃, CH₃OH, and CH₃O are now above or similar to the detected gas phase values.

The synthesis of methyl formate HCOOCH₃ depends on both HCO and CH₃O radicals. We found it impossible to achieve a sufficiently high ice abundance for HCOOCH₃ with changes in E_A for reactions 17, 18, and 19. Thus, the calculated relative ice abundance for this molecule remains approximately four orders of magnitude below the observed gas-phase values, which are between 10^{-11} and 10^{-9} (Öberg et al. 2010; Bacmann et al. 2012; Cernicharo et al. 2012).

Methyl formate is also inefficiently produced in several other models considering either starless or

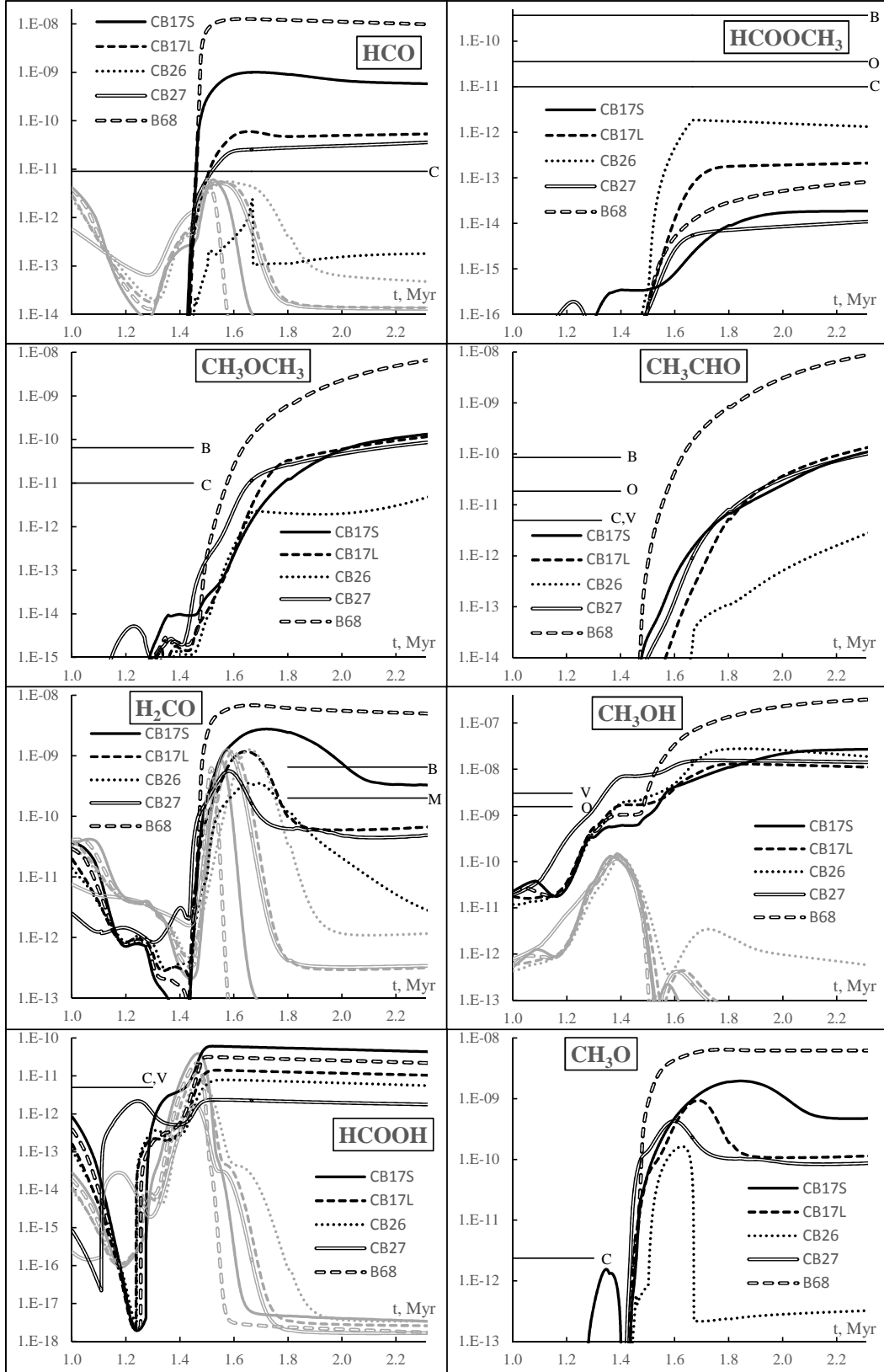


Fig. 18.— Calculated abundances, relative to H, of selected organic molecules for the Compromise model. Gray lines: gas-phase abundance; black lines: abundance in ice (surface and three mantle sublayers). For references see the caption of figure 14.

Table 6: Changes in reaction data for the compromise model.

No.	Reaction	Activation barrier E_A , K		
		Standard ^a	Fuchs et al. (2009)	Compromise
17	$\text{H} + \text{CO} \rightarrow \text{HCO}$	2500	390-520	1600
18	$\text{H} + \text{H}_2\text{CO} \rightarrow \text{CH}_3\text{O}$	2100	415-490	415
19	$\text{H} + \text{H}_2\text{CO} \rightarrow \text{CH}_2\text{OH}$	2500	415-490	415

^aThe initial values used in this paper

prestellar cores (Garrod 2013; Vasyunin & Herbst 2013a,b). Chang & Herbst (2014) are able to efficiently synthesize HCOOCH_3 with a Monte-Carlo model, but their results also show a likely excess of CH_4 and a shortage of CO_2 – discrepancies generally not observed in the abovementioned other models. These results may indicate that the inefficient synthesis of HCOOCH_3 is not an artifact, caused by the limits of the present study. A higher temperature may be necessary for an efficient synthesis of HCOOCH_3 , as suggested by Garrod & Herbst (2006).

5.2.3. Chemistry differences with the Standard model

The most significant abundance increase for the CH_3O group is observed in the B 68 model. First, the lower temperatures in this core mean a low mobility for atomic H in ice. Second, the abundant CO is now more easily hydrogenated, thanks to the lower E_A and CO soaks up much of the available atomic hydrogen in the mantle. These two factors result an accumulation of radicals so that they have greater chance to react with other multi-atom species. For the present discussion on COMs, the most important radicals are CH_3O and HCO . The effect is especially visible for B 68 and CB 17 S.

For species that are formed via HCO , the situation is less clear because formaldehyde H_2CO is consumed by reactions 18 and 19. In cores CB 17 L and CB 27, formaldehyde has its maximum ice abundance decreased below the detected gas-phase values. A similar situation can be observed for formic acid HCOOH , directly related to HCO .

Figure 19 shows that in the compromise model the abundances of COMs are increased in all sub-

layers (cf. figures 16 and 17). The main part of their synthesis still occurs in the outer sublayer 1. Species whose synthesis involve CH_3O and CH_3 , do not reach a steady abundance until the end of the simulation, mainly because they can be regarded as the end products of CO hydrogenation sequence.

5.3. The synthesis of COMs in ice in a temporal warm-up event

The discussion in the above section 5.2.2 shows that for some COMs (notably, methyl formate) the calculated abundances are nowhere near their observed values. To test how a mild and temporal warm-up event can affect the ice abundances of COMs, we used the B 68 Compromise model that undergoes a temperature increase to 20K for 1kyr at $t = 1.6\text{Myr}$.

5.3.1. Chemistry differences with previous models

Figures 20 and 21 show that the temperature spike positively affects the production of a number of solid species – HCOOCH_3 , CH_2CCO , CH_2CO , NH_2CHO , C_2H_2 , CH_4 . Notably, the gas phase abundance is substantially increased for species synthesized on the surface – CH_2CCO , H_2CO , NH_2CN , C_2H_2 , CH_3CN , CH_2NH , and CH_4 , thanks to reactive desorption.

For most species, the changes in ice abundance are within one order of magnitude. However, for methyl formate HCOOCH_3 and formamide NH_2CHO an increase by approximately five and three orders of magnitude is observed, respectively. We therefore explore deeper the temperature spike-induced chemistry of these two species. Initiated at 1.6Myr, the rise of abundances actually occurs over a period of 100kyr after the tem-

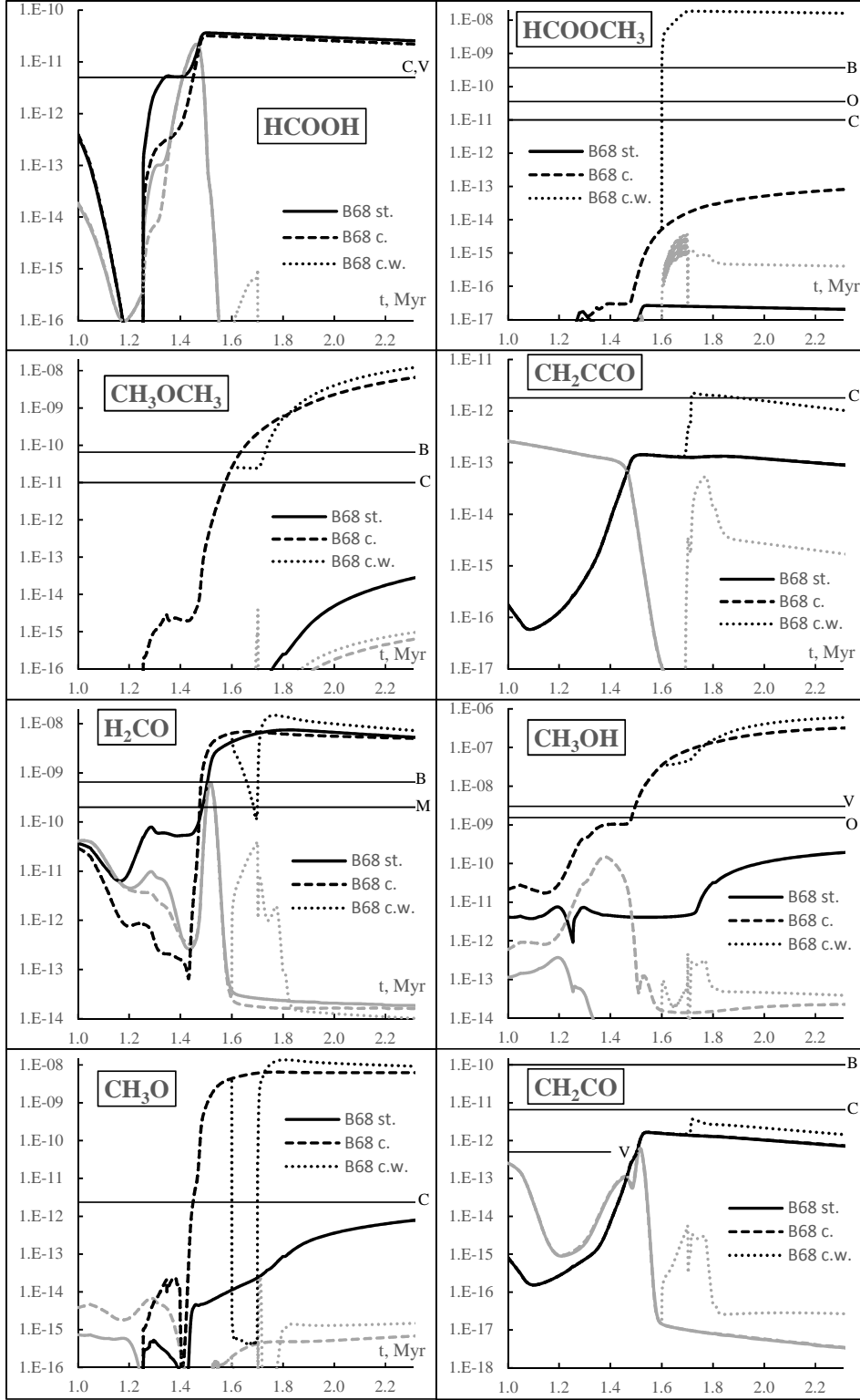


Fig. 20.— Comparison of calculated COM abundances, relative to H , for the B 68 core between the Standard model (st.), Compromise model (c.), and Compromise model with a warm temperature spike (c.w.), set No. 1. The two latter models begin to show differences only after 1.6 Myr, when the temperature spike occurs. References as in figure 14.

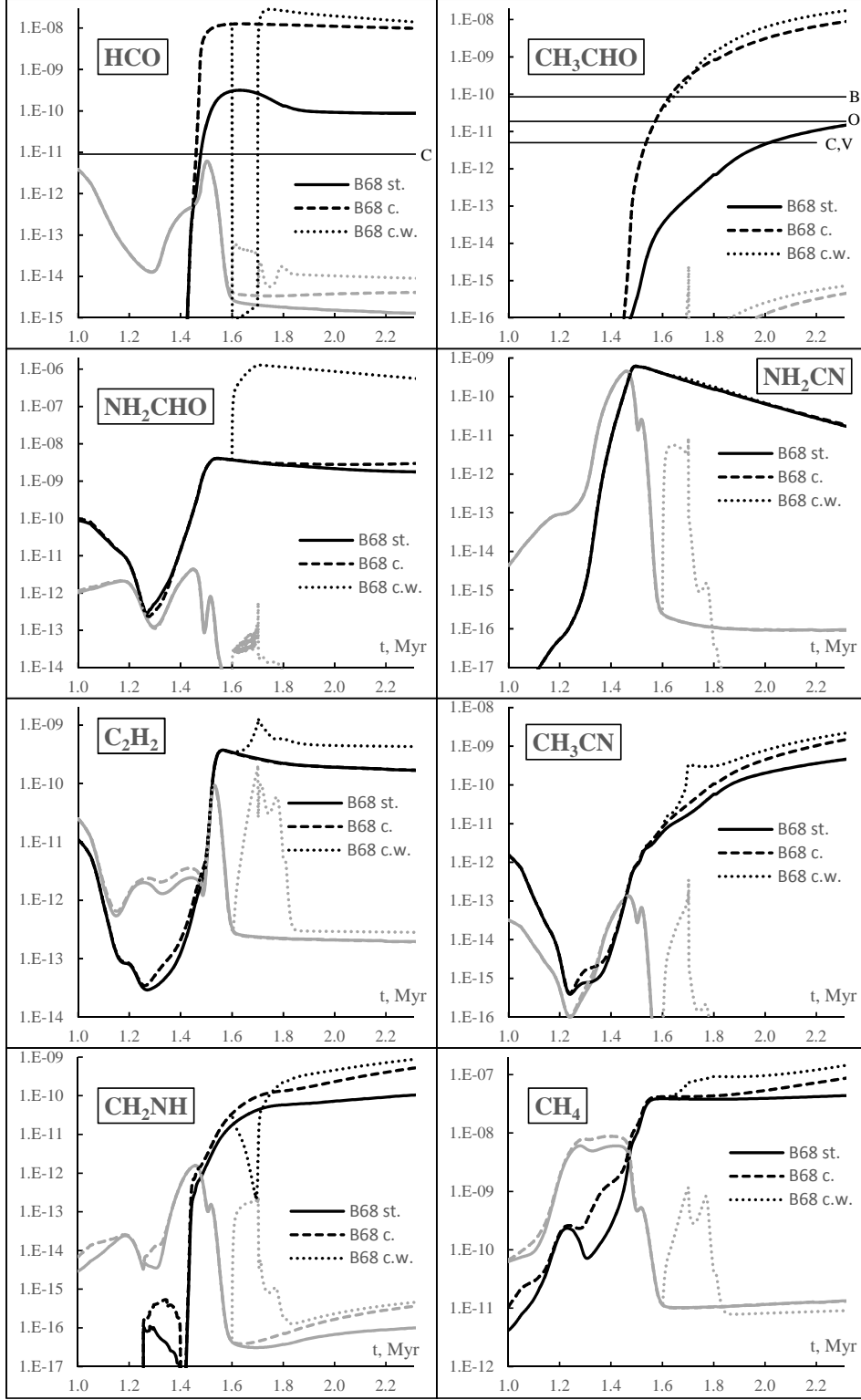


Fig. 21.— Comparison of calculated COM abundances, relative to H, for the B 68 core between the standard model (st.), compromise model (c.), and compromise model with a warm temperature spike (c.w.) at 1.6Myr, set No. 2. References as in figure 14.

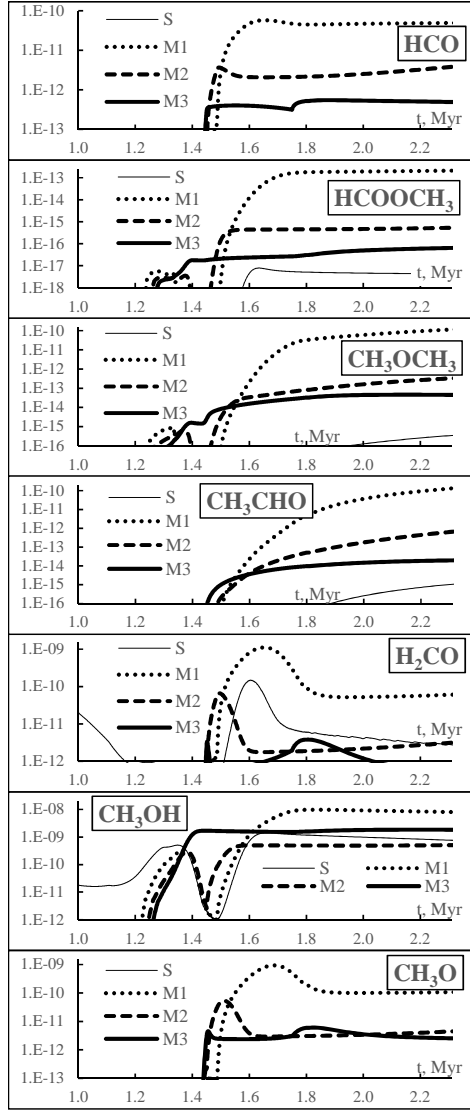


Fig. 19.— Calculated abundances, relative to H, in ice sublayers for selected organic molecules, Compromise model, CB 17 L core.

perature spike. Figure 22 shows the abundances of NH_2CHO and HCOOCH_3 in ice sublayers.

Methyl formate production occurs mainly in the middle sublayer 2. This is unlike most other COMs in the Standard and Compromise models that are synthesized in the outer sublayer 1 (figure 19). Sublayer 2 is the only one that is rich in both, CO and H_2O . The former is the source species for HCO and CH_3O radicals that combine into HCOOCH_3 . Meanwhile, the photodissociation of water is the principal source of atomic hydrogen, necessary for the hydrogenation sequence $\text{CO} \rightarrow \text{HCO} \rightarrow \text{H}_2\text{CO} \rightarrow \text{CH}_3\text{O}; \text{CH}_2\text{OH}$. Thus, CO hydrogenation by the mobile H atoms at the 20K spike, followed by combination of HCO and $\text{CH}_3\text{O} \approx 100\text{kyr}$ after the spike, is the main mechanism for the formation of HCOOCH_3 .

The case of formamide is different – NH_2CHO reaches similar abundance in all three sublayers after the 20K spike. This is because in none of the sublayers its main parent species – CO and NH_3 – both have a high abundance. While NH_3 is mainly concentrated in sublayer 3, CO is abundant only in sublayers 1 and 2.

5.3.2. Discussion on temperature spike model results

The ice abundance increases occur because diffusion, proximity, and activation energy barriers are more effectively overcome at 20K. The subsequent reactions temporarily reduce of ice abundances for the radical species HCO, CH_3O , and CH_2OH . The results shown in figures 20 and 21

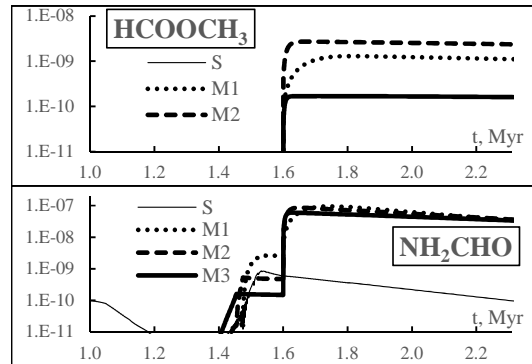


Fig. 22.— Calculated abundances, relative to H, in ice sublayers for species most affected by a 1kyr 20K temperature spike in the Compromise model for the B 68 core.

suggest that even such a small and short warm-up period is sufficient to qualitatively reproduce the abundance of methyl formate in ice and that the ice abundances of other organic species do not become disbalanced. The single-point 0D approach used in the model prevents a quantitative comparison between calculation results and observations.

We suggest two likely causes for a (temporal) temperature increase for a portion of ices in a starless or prestellar core. First, the gas parcel can be exposed to the interstellar radiation because of turbulent motions in the core, as suggested by Boland & de Jong (1982) and Martinell et al. (2006). Second, low-velocity transient shocks within the core (Williams & Hartquist 1984) may also result in mild heating of the gas. Both of these mechanisms also offer a hypothesis for the desorption mechanism – either photodesorption or collisional sputtering of the weakly-bound, non-polar ice outer layers. These considerations are supported by the turbulent motions observed in starless cores (Redman et al. 2006; Levshakov et al. 2014; Steinacker et al. 2014).

6. Summary

A model that describes ices in a detailed way was used to investigate ice chemistry in five different examples of starless cores. While the importance of subsurface ice chemistry has been noted in previous studies (Cuppen & Herbst 2007; Kalvāns & Shmeld 2010; Garrod 2013), the most general conclusion from the present study is that chemical processes in ice depend strongly on the particular (sub)layer, where the molecules in consideration are located. This arises because of variations in abundances of major ice components (H_2O , CO , CO_2 , N_2 , NH_3) in different layers on the same grains. This conclusion is in line with the results of a prestellar core model (Paper II) and a pseudo-time dependent Monte Carlo model by (Chang & Herbst 2014). Single sublayer approach (Kalvāns & Shmeld 2010, 2013; Garrod 2013; Belloche et al. 2014) is not suitable for representing subsurface chemistry of interstellar ices. This is especially so if the synthesis of minor species is studied.

The H_2O and CO ices in dark cores are photoprocessed to CO_2 via sequence (4). This sets limits to core lifetimes, because current observa-

tions indicate that the $\text{CO}_2:\text{H}_2\text{O}$ abundance ratio in ice likely is 44% or less (Boogert et al. 2011). The maximum lifetime for a quiescent and stable molecular core with constant physical conditions (Phase 2) inferred this way in the present model is 650kyr (CB 17 S core). It is hard to pinpoint a precise value because of the limitations in the physical model, and uncertainties regarding the turbulence in dark cores. Taking this into account we can state that the model indicates dark core lifetimes of $<1\text{Myr}$. The lower $\text{CO}_2:\text{H}_2\text{O}$ ratio in Taurus (Whittet et al. 2007) may indicate that these starless cores may be younger than those in most other molecular clouds, observed by Boogert et al. (2011) and Öberg et al. (2011).

The $\text{H}_2\text{O}:\text{CO}$ ice abundance ratio cannot be used as reliable indicator of core age because CO resides mostly on the outer surface of the grains. There, it can be rather easily lost to the gas phase or converted into other species in mild heating events. Such processes can be induced by exposure to interstellar photons or low-velocity shocks within the core, as discussed below.

Because of more efficient desorption, the present model predicts shorter and higher abundance peaks during the cloud collapse phase (or ice formation epoch) for a number of species produced in dense gas or on the surface (section 3.3). These include H_2O , CO_2 , NH_3 , H_2O_2 , H_2S , SO , SO_2 , OCS , HCOOH , H_2CO , CH_2CO , CH_4 , O_2 , H_2S_2 , N_2 etc.

We find that O_2 and H_2O_2 are the main oxygen reservoirs in ice, except water and carbon oxides. O_2 forms in the gas and on the surface, and is being converted into the H_2O_2 via photoprocessing in subsurface ice. It was suggested that H_2O_2 and O_2H reach their gas-phase abundance peaks during the freeze out epoch, thanks to an active molecular exchange between the gas and the surface. The principal cause of desorption, necessary for this exchange, is irradiation by interstellar photons.

Calculations show that the $\text{HNC}:\text{HCN}$ ratio in ice can be as high as 1.75 (in CB 27 core model), while it remains close to or below unity in the gas phase. Sulfur in ice is roughly equally divided between reduced (H_2S) and oxidized (SO) forms. Subsurface processing of these sulfur species gives rise to OCS , NS , and H_2CS , indicating an interesting diversity for the sulfur chemistry.

Investigating the chemistry of COMs, we found that lower activation energies – more consistent with experimentally detected values – for hydrogenation reactions of CO and H₂CO may help explaining the observations of COMs in the interstellar medium. A mild and temporal warm-up event helps to produce an abundance of methyl formate in ice that is higher and more consistent with gas-phase HCOOCH₃ observations. Such an event also substantially increases the ice abundance of formamide.

Desorption by interstellar photons and ice sputtering in grain collisions may transport the COMs to the gas phase. Both of these mechanisms require either turbulence within the cores or external influence. These findings are probably supported by the fact that two of the dense cores with detected COMs – L1689b (Bacmann et al. 2012) and B1-b (Marcelino et al. 2005; Öberg et al. 2010; Cernicharo et al. 2012) – have nearby star-formation regions (Kirk et al. 2007; Öberg et al. 2010), while the third, L1544 (Vastel et al. 2014), is known to be turbulent and on the verge of collapse (Caselli et al. 2002; Tatematsu et al. 2014).

I acknowledge the support of Ventspils City Council. This research has made use of NASA's Astrophysics Data System. I thank the anonymous referee for many useful suggestions that improved the paper.

REFERENCES

- Acharyya, K., Hassel, G. E., & Herbst, E. 2011, *ApJ*, 732, 73
- Adams, F. C., & Shu, F. H. 2007, *ApJ*, 671, 497
- Aikawa, Y., Ohashi, N., Inutsuka, S.-i., Herbst, E., & Takakuwa, S. 2001, *ApJ*, 552, 639
- Allen, M., & Robinson, G. W. 1977, *ApJ*, 212, 396
- Andersson, S., Al-Halabi, A., Kroes, G.-J., & van Dishoeck, E. F. 2006, *JChPh*, 124, 064715
- Andersson, S., & van Dishoeck, E. F. 2008, *A&A*, 491, 907
- Awad, Z., Chigai, T., Kimura, Y., Shalabiea, O. M., & Yamamoto, T. 2005, *ApJ*, 626, 262
- Awad, Z., Viti, S., Bayet, E., & Caselli, P. 2014, *MNRAS*, 443, 275
- Bacmann, A., Taquet, V., Faure, A., Kahane, C., & Ceccarelli, C. 2012, *A&A*, 541, L12
- Belloche, A., Garrod, R. T., Müller, H. S. P., & Menten, K. M. 2014, *Science*, 345, 1584
- Bergin, E. A., & Langer, W. D. 1997, *ApJ*, 486, 316
- Bergin, E. A., Maret, S., van der Tak, F. F. S., et al. 2006, *ApJ*, 645, 369
- Bergman, P., Parise, B., Liseau, R., et al. 2011, *A&A*, 531, L8
- Boland, W., & de Jong, T. 1982, *ApJ*, 261, 110
- Boogert, A. C. A., Huard, T. L., Cook, A. M., et al. 2011, *ApJ*, 729, 92
- Brown, P. D. 1990, *MNRAS*, 243, 65
- Brown, P. D., Charnley, S. B., & Millar, T. J. 1988, *MNRAS*, 231, 409
- Brown, P. D., & Millar, T. J. 1989, *MNRAS*, 237, 661
- Caselli, P., Benson, P. J., Myers, P. C., & Tafalla, M. 2002, *ApJ*, 572, 238
- Caselli, P., Keto, E., Bergin, E. A., et al. 2012, *ApJ*, 759, L37
- Cernicharo, J., Marcelino, N., Roueff, E., et al. 2012, *ApJ*, 759, L43
- Chang, Q., & Herbst, E. 2014, *ApJ*, 787, 135
- Crapsi, A., Caselli, P., Walmsley, M. C., & Tafalla, M. 2007, *A&A*, 470, 221
- Cuppen, H. M., & Herbst, E. 2007, *ApJ*, 668, 294
- D'Hendecourt, L. B., Allamandola, L. J., & Greenberg, J. M. 1985, *A&A*, 152, 130
- Dominik, C., Ceccarelli, C., Hollenbach, D., & Kaufman, M. 2005, *ApJ*, 635, L85
- Du, F., Parise, B., & Bergman, P. 2012, *A&A*, 538, A91
- Fuchs, G. W., Cuppen, H. M., Ioppolo, S., et al. 2009, *A&A*, 505, 629
- Garrod, R. T. 2013, *ApJ*, 765, 60
- Garrod, R. T., & Herbst, E. 2006, *A&A*, 457, 927
- Garrod, R. T., & Pauly, T. 2011, *ApJ*, 735, 15
- Garrod, R. T., Wakelam, V., & Herbst, E. 2007, *A&A*, 467, 1103
- Garrod, R. T., Weaver, S. L. W., & Herbst, E. 2008, *ApJ*, 682, 283
- Gibb, E. L., Whittet, D. C. B., Boogert, A. C. A., & Tielens, A. G. G. M. 2004, *ApJS*, 151, 35
- Goldsmith, P. F., Li, D., Bergin, E. A., et al. 2002, *ApJ*, 576, 814
- Green, N. J. B., Toniazzi, T., Pilling, M. J., et al. 2001, *A&A*, 375, 1111
- Hartmann, L. 2009, *Accretion Processes in Star Formation: Second Edition* (Cambridge University Press)
- Hasegawa, T. I., & Herbst, E. 1993a, *MNRAS*, 261, 83
- . 1993b, *MNRAS*, 263, 589
- Hasegawa, T. I., Herbst, E., & Leung, C. M. 1992, *ApJS*, 82, 167
- Hirota, T., Yamamoto, S., Mikami, H., & Ohishi, M. 1998, *ApJ*, 503, 717
- Kalvāns, J. 2015a, *A&A*, 573, A38
- . 2015b, accepted for publication in *ApJ*

- Kalvāns, J., & Shmeld, I. 2010, *A&A*, 521, A37
- . 2013, *A&A*, 554, A111
- Karssemeijer, L. J., & Cuppen, H. M. 2014, *A&A*, 569, A107
- Keto, E., & Caselli, P. 2010, *MNRAS*, 402, 1625
- Kirk, J. M., Ward-Thompson, D., & André, P. 2007, *MNRAS*, 375, 843
- Laas, J. C., Garrod, R. T., Herbst, E., & Widicus Weaver, S. L. 2011, *ApJ*, 728, 71
- Larsson, B., Liseau, R., Pagani, L., et al. 2007, *A&A*, 466, 999
- Launhardt, R., Nutter, D., Ward-Thompson, D., et al. 2010, *ApJS*, 188, 139
- Lee, H.-H., Herbst, E., Pineau des Forets, G., Roueff, E., & Le Bourlot, J. 1996, *A&A*, 311, 690
- Lee, J.-E., Bergin, E. A., & Evans, II, N. J. 2004, *ApJ*, 617, 360
- Levshakov, S. A., Henkel, C., Reimers, D., & Wang, M. 2014, *A&A*, 567, A78
- Li, X., Heays, A. N., Visser, R., et al. 2013, *A&A*, 555, A14
- Lippok, N., Launhardt, R., Semenov, D., et al. 2013, *A&A*, 560, A41
- Liseau, R., Larsson, B., Bergman, P., et al. 2010, *A&A*, 510, A98
- Marcelino, N., Cernicharo, J., Roueff, E., Gerin, M., & Mauersberger, R. 2005, *ApJ*, 620, 308
- Maret, S., Bergin, E. A., & Tafalla, M. 2013, *A&A*, 559, A53
- Martinell, J. J., Del-Castillo-Negrete, D., Raga, A. C., & Williams, D. A. 2006, *MNRAS*, 372, 213
- Mokrane, H., Chaabouni, H., Accolla, M., et al. 2009, *ApJ*, 705, L195
- Nejad, L. A. M., Williams, D. A., & Charnley, S. B. 1990, *MNRAS*, 246, 183
- Öberg, K. I., Boogert, A. C. A., Pontoppidan, K. M., et al. 2011, *ApJ*, 740, 109
- Öberg, K. I., Bottinelli, S., Jørgensen, J. K., & van Dishoeck, E. F. 2010, *ApJ*, 716, 825
- Parise, B., Bergman, P., & Du, F. 2012, *A&A*, 541, L11
- Pickles, J. B., & Williams, D. A. 1977a, *ApSS*, 52, 443
- . 1977b, *Ap&SS*, 52, 453
- Plummer, H. C. 1911, *MNRAS*, 71, 460
- Rawlings, J. M. C., Hartquist, T. W., Menten, K. M., & Williams, D. A. 1992, *MNRAS*, 255, 471
- Reboussin, L., Wakelam, V., Guilloteau, S., & Hersant, F. 2014, *MNRAS*, 440, 3557
- Redman, M. P., Keto, E., & Rawlings, J. M. C. 2006, *MNRAS*, 370, L1
- Roser, J. E., Vidali, G., Manicò, G., & Pirronello, V. 2001, *ApJ*, 555, L61
- Ruffle, D. P., Hartquist, T. W., Caselli, P., & Williams, D. A. 1999, *MNRAS*, 306, 691
- Ruffle, D. P., & Herbst, E. 2001b, *MNRAS*, 324, 1054
- Ruoskanen, J., Harju, J., Juvela, M., et al. 2011, *A&A*, 534, A122
- Scappini, F., Cecchi-Pestellini, C., Smith, H., Klemperer, W., & Dalgarno, A. 2003, *MNRAS*, 341, 657
- Schmalzl, M., Launhardt, R., Stutz, A. M., et al. 2014, *A&A*, 569, A7
- Semenov, D., Hersant, F., Wakelam, V., et al. 2010, *A&A*, 522, A42
- Steinacker, J., Ormel, C. W., Andersen, M., & Bacmann, A. 2014, *A&A*, 564, A96
- Taquet, V., Ceccarelli, C., & Kahane, C. 2012, *A&A*, 538, A42
- Taquet, V., Charnley, S. B., & Sipilä, O. 2014, *ApJ*, 791, 1
- Tatematsu, K., Hirota, T., Ohashi, S., et al. 2014, *ApJ*, 789, 83
- Tielens, A. G. G. M., & Hagen, W. 1982, *A&A*, 114, 245
- Turner, B. E. 1998, *ApJ*, 501, 731
- Vastel, C., Ceccarelli, C., Lefloch, B., & Bachiller, R. 2014, *ApJ*, 795, L2
- Vasyunin, A. I., & Herbst, E. 2013a, *ApJ*, 762, 86
- . 2013b, *ApJ*, 769, 34
- Viti, S., & Williams, D. A. 1999, *MNRAS*, 305, 755
- Wakelam, V., & Herbst, E. 2008, *ApJ*, 680, 371
- Watson, W. D., & Salpeter, E. E. 1972, *ApJ*, 174, 321
- Whittet, D. C. B., Gerakines, P. A., Hough, J. H., & Shenoy, S. S. 2001, *ApJ*, 547, 872
- Whittet, D. C. B., Shenoy, S. S., Bergin, E. A., et al. 2007, *ApJ*, 655, 332
- Whitworth, A. P., & Ward-Thompson, D. 2001, *ApJ*, 547, 317
- Williams, D. A., & Hartquist, T. W. 1984, *MNRAS*, 210, 141
- Woon, D. E. 2002, *ApJ*, 569, 541

This 2-column preprint was prepared with the AAS L^AT_EX macros v5.2.